CELL BIOLOGY

The PP2A-B55α phosphatase is a master regulator of mitochondrial degradation and biogenesis

Valentina Cianfanelli[1,2]*, Monica Nanni[3]†, Samantha Corrà[4]‡, Sofia Mauri[4], David Sumpton[5], Sergio Lilla[5], Rossella De Cegli[6], Matteo Bordi[7], Giacomo Milletti[8], Caterina Ferraina[2], Arnaldur Hall[9], Michele Petraroia[1], Valentina Clausi[1,2], Ezio Giorda[10], Marco Scarsella[10], Alessandra Barbiera[2], Giulia Cadeddu[11], Marco Colasanti[1], Tiziana Persichini[1], Kenji Maeda[12], Apolinar Maya-Mendoza[8], Jiri Bartek[9,13], Chiara Di Malta[6,14], Franco Locatelli[15,16], Sara Zanivan[5,17]§, Shehab Ismail[18], Elena Ziviani[4], Francesco Cecconi[7,19]¶*

Mitochondrial homeostasis relies on a tight balance between mitochondrial biogenesis and degradation. Although mitophagy is one of the main pathways involved in the clearance of damaged or old mitochondria, its coordination with mitochondrial biogenesis is poorly characterized. Here, by unbiased approaches including last-generation liquid chromatography coupled to mass spectrometry and transcriptomics, we identify the protein phosphatase PP2A-B55α/PPP2R2A as a Parkin-dependent regulator of mitochondrial number. Upon mitochondrial damage, PP2A-B55α determines the amplitude of mitophagy induction and execution by regulating both early and late mitophagy events. A few minutes after the insult, ULK1 is released from the inhibitory regulation of PP2A-B55α, whereas 2 to 4 hours later, PP2A-B55α promotes the nuclear translocation of TFEB, the master regulator of autophagy and lysosome genes, to support mitophagy execution. Moreover, PP2A-B55α controls a transcriptional program of mitochondrial biogenesis by stabilizing the Parkin substrate and PGC-1α inhibitor PARIS. PP2A-B55α targeting rescues neurodegenerative phenotypes in a fly model of Parkinson's disease, thus suggesting potential therapeutic application.

INTRODUCTION

Macroautophagy, hereafter autophagy, is a conserved catabolic pathway responsible for cellular homeostasis maintenance, as well as for coping with stress conditions (*1*). The autophagy pathways that selectively target single cellular components for degradation are referred to as selective autophagy, a process that is further subdivided according to the degraded cargo, e.g., single proteins or protein aggregates, lipid droplets, pathogens, and organelles. Among different types of selective autophagy, the one executing organelle turnover is probably the most intensively studied because of its crucial relevance for cellular homeostasis and involvement in the etiology of numerous human diseases, from cancer to neurodegeneration (*2*). The selective autophagy of mitochondria, termed mitophagy, targets damaged, dysfunctional, or old mitochondria to maintain mitochondrial homeostasis, in a balance with mitochondrial biogenesis, which replenishes the mitochondrial pool after degradation (*3*, *4*). The mitophagy pathways can be subdivided into ubiquitin-dependent and -independent mechanisms. The former pathway relies on E3 ubiquitin ligases responsible for decorating the targeted mitochondria with ubiquitin molecules, thereby providing the "eat me" signal for ubiquitin-dependent mitophagy. The E3 ligase Parkin is probably the most studied in the mitophagy field, and in the models expressing Parkin, this enzyme is among the drivers of mitophagy initiation (*5*). Other enzymes highly relevant to mitophagy initiation and execution are Ser/Thr protein kinases, which regulate Parkin activity, the recruitment of the autophagosome machinery at damaged mitochondria, and the affinity of the selective autophagy receptors for the ubiquitinated cargo, as well as for the family members of the mammalian Autophagy-Related Gene 8 (mATG8) (*6*–*11*). The binding between the receptors and mATG8s contributes to the engulfment of the damaged mitochondria into the autophagy vesicle, the autophagosome, whose fusion with the lysosome strictly depends on mATG8s (*12*). Among the autophagy kinases relevant to mitophagy initiation and execution is Unc-51–Like Kinase 1 (ULK1), which is activated upon mitochondrial damage (*10*, *11*). On the other hand, several factors are known to control mitochondrial biogenesis, in a continuous cross-talk with the processes regulating mitochondrial dynamics and functions (*13*, *14*). The transcriptional coactivator peroxisome proliferator-activated receptor-γ coactivator-1α (PGC-1α) is prominent among such factors, playing a key role in promoting the

---

[1]Department of Science, University "Roma TRE", Rome, Italy. [2]Gynecologic Oncology Unit, Department of Woman and Child Health and Public Health, Fondazione Policlinico Universitario Agostino Gemelli IRCCS, Rome, Italy. [3]Department of Clinical and Molecular Medicine, Sapienza University of Rome, Rome, Italy. [4]Department of Biology, University of Padua, Padua, Italy. [5]Cancer Research UK Scotland Institute, Glasgow, UK. [6]Telethon Institute of Genetics and Medicine (TIGEM), Pozzuoli, Italy. [7]Dipartimento di Scienze Biotecnologiche di Base, Cliniche Intensivologiche e Perioperatorie, Università Cattolica del Sacro Cuore, Rome, Italy. [8]DNA Replication and Cancer Group, Danish Cancer Institute, Copenhagen, Denmark. [9]Genome Integrity Group, Danish Cancer Institute, Copenhagen, Denmark. [10]Research Laboratories, Bambino Gesù Children's Hospital, IRCCS, Rome, Italy. [11]PhD Program in Cellular and Molecular Biology, Department of Biology, University of Rome "Tor Vergata," Rome, Italy. [12]Cell Death and Metabolism, Center for Autophagy, Recycling and Disease (CARD), Danish Cancer Institute, Copenhagen, Denmark. [13]Division of Genome Biology, Department of Medical Biochemistry and Biophysics, Science for Life Laboratory, Karolinska Instituttet, Stockholm, Sweden. [14]Medical Genetics Unit, Department of Medical and Translational Science, Federico II University, Naples, Italy. [15]Department of Onco-Haematology and Cell and Gene Therapy, Bambino Gesù Children's Hospital, IRCCS, Rome, Italy. [16]Department of Life Sciences and Public Health, Catholic University of the Sacred Heart, Rome, Italy. [17]School of Cancer Sciences, University of Glasgow, Glasgow, United Kingdom. [18]Biochemistry, Molecular and Structural Biology, Department of Chemistry, KU Leuven, Leuven, Belgium. [19]Fondazione Policlinico Universitario Agostino Gemelli IRCCS, Rome, Italy.
*Corresponding author. Email: francesco.cecconi@unicatt.it (F.C.); valentina.cianfanelli@uniroma3.it (V.C.)
†Present address: Department of Pathology, University of California San Francisco, CA, USA.
‡Present address: Veneto Institute of Molecular Medicine (VIMM), Padua, Italy.
§Present address: University of Texas MD Anderson Cancer Center, Houston, Texas, USA.
¶Last author.

expression of mitochondrial genes and promptly responding to a number of nutritional and metabolic signals (*15*).

Overall, while kinases actively regulate all aspects of mitochondrial homeostasis, little is known about the corresponding phosphatases, which control reversible phosphorylation events, enabling cells to respond to different and often divergent stimuli in a very short time. Here, we unveil a role for the Protein Phosphatase 2A (PP2A) regulatory subunit B55α in the holistic control of dephosphorylation events crucial to mitochondrial number regulation, describing three previously uncharacterized potential targets of its activity and analyzing its effects in vitro and in vivo.

RESULTS

PP2A-B55α dephosphorylates ULK1 at S556

The AMP-activated protein Kinase (AMPK)-dependent phosphorylation of ULK1 is a crucial event in the selective clearance of mitochondria through autophagy. In particular, AMPK phosphorylates ULK1 at serine 556 (S556; mouse 555), resulting in mitophagy induction under conditions such as hypoxia, acute exercise, and mitochondrial damage (*16*–*19*). As observed for other mitophagy regulatory events, ULK1 phosphorylation at S556 is highly dynamic. However, as of today, the protein phosphatase(s) targeting this phosphorylation site (phospho-site) are unknown. To identify the involved phosphatase, we first tested the sensitivity of S556 to acute phosphatase inhibition by treating HeLa cells with okadaic acid (Ok. Ac.), an inhibitor of serine/threonine protein phosphatases. The treatment with Ok. Ac. enhanced ULK1 phosphorylated at S556 (P-ULK1 S556), while the degree of phosphorylation at the inhibitory phospho-site of ULK1, S757, remained unaffected by such treatment (Fig. 1, A and B, and fig. S1, A and B). Ok. Ac. inhibits multiple protein phosphatases of the PPP family, among which PP2A is the most abundant and ubiquitously expressed (*20*). Moreover, PP2A functionally interacts with ULK1 to regulate starvation-induced autophagy (*21*, *22*). Therefore, we tested the impact of this phosphatase on P-ULK1 S556 by knocking down PP2Ac, the catalytic subunit of PP2A. Similar to what we observed upon Ok. Ac. treatment, PP2Ac depletion increased ULK1 phosphorylation at S556 without affecting S757 phosphorylation (Fig. 1C and fig. S1, C and D). Likewise, recombinant PP2Ac dephosphorylated P-ULK1 S556, but not S757, in an in vitro phosphatase assay (Fig. 1, D and E). Together, these results show that PP2A targets ULK1 phospho-site S556, which is phosphorylated by AMPK, while manipulation of PP2A does not affect the mammalian Target Of Rapamycin Complex 1 (mTORC1)–targeted phosphorylation of ULK1 at S757, a modification probably regulated by a distinct phosphatase.

PP2A is a multifunctional phosphatase subjected to tight regulation in the cell. The active form of PP2A is a heterotrimeric complex, consisting of PP2Ac, the scaffolding subunit (PR65), and one of the variable regulatory subunits that confers substrate specificity and thus dictates the biological function of PP2A (*23*–*25*). Because multiple regulatory subunits are expressed at the same time in mammalian cells, a multitude of PP2A complexes coexist and target different substrates. To identify the regulatory subunit of PP2A targeting P-ULK1 S556, we exploited an unbiased approach, coupling last-generation chromatography techniques to Liquid Chromatography–Mass Spectrometry (LC-MS) proteomics (Fig. 1F). First, we performed biochemical fractionation in a series of seven chromatographic steps using the protein extracts of ULK1/2 double knockout (DKO) murine embryonic fibroblasts (MEFs; Fig. 1F) as the source material. Fractions from each step of purification were analyzed for their phosphatase activity against ULK1 by first incubating each fraction with the immunoprecipitated ULK1 and then assessing their capability to dephosphorylate S556 using a specific antiphospho antibody by Western blot analysis. Next, the fractions capable of dephosphorylating the exogenous P-ULK1 S556 substrate were combined as input for the next purification step (Fig. 1F). Results from the last column (gel filtration) are shown in Fig. 1G. The chromatogram of the fractions collected showed the presence of proteins in several fractions, in agreement with the SDS–polyacrylamide gel electrophoresis (PAGE), followed by SYPRO protein gel staining, performed on a small quantity of fractions (9 to 21; fig. S1E). All fractions (1 to 24) collected from the last column were then tested for their phosphatase activity toward P-ULK1. The results showed fractions nos. 13 to 18 as the only ones capable of dephosphorylating P-ULK1 S556 (Fig. 1G), indicating that those fractions contain the PP2A complex responsible for ULK1 dephosphorylation. LC-MS proteomics of all fractions collected from the last column (1 to 24) was also run, and an aliquot of each fraction was submitted separately to trypsin digestion and analyzed using MS. A total of 132 proteins was quantified from all fractions analyzed (table S1). Among them, we identified only one complex of PP2A present in the fractions active against P-ULK1 S556, namely, PP2A-B55α, which consists of the scaffolding subunit PR65A (gene name Ppp2r1a), the catalytic subunit (gene name: Ppp2ca/Ppp2cb), and, notably, the B55α regulatory subunit (gene name: Ppp2r2a) that dictates the substrate specificity of the complex (fig. S1F). In agreement with the proteomics results, knockdown of the scaffolding subunit PR65A, but not its closely related isoform PR65B (*26*), increased P-ULK1 S556 levels (fig. S1, G and H).

Next, to validate the relevance of B55α in ULK1 regulation in cells, we knocked down B55α in HeLa cells induced for Parkin expression, a well-established model to study Parkin-dependent mitophagy (*27*). To induce mitophagy, we treated cells with oligomycin and antimycin A (OA), treatments that trigger mitochondrial damage, AMPK activation, and consequent phosphorylation of ULK1 at S556. Consistent with its ability to dephosphorylate ULK1 in vitro (Fig. 1G), B55α depletion resulted in increased P-ULK1 S556 levels upon OA treatment (Fig. 1, H and I), thus demonstrating that the phosphorylation state of ULK1 S556 depends on the coordinated activity of its kinase, AMPK, and phosphatase, PP2A-B55α. Because B55α knockdown does not affect AMPK activity (Fig. 1, H and J), its effect on P-ULK1 S556 is most likely direct, in agreement with the in vitro results (Fig. 1G). Upon mitochondrial damage, we also monitored the phosphorylation of mTOR-targeted S638, which was insensitive to the expression levels of B55α (Fig. 1, H and K), despite this site being previously identified as a B55α target upon starvation (*16*, *21*, *28*). Notably, while B55α depletion increased P-ULK1 S556 levels, expression of exogenous Yellow Fluorescent Protein (YFP)–B55α restored them to baseline after 30 min of OA treatment (Fig. 1, L and M). Together, our results thus show that PP2A-B55α restrains ULK1 phosphorylation at S556 under basal conditions and upon mitochondrial damage (Fig. 1N), while most likely other phosphatase(s) may dephosphorylate ULK1 at different phospho-sites.

PP2A-B55α inhibits mitochondria priming for recognition by the autophagy machinery

To be selectively recognized and degraded by autophagy, damaged mitochondria must be primed by "eat me" signals and autophagy receptors. In Parkin-competent models, the prominent "eat me" signals

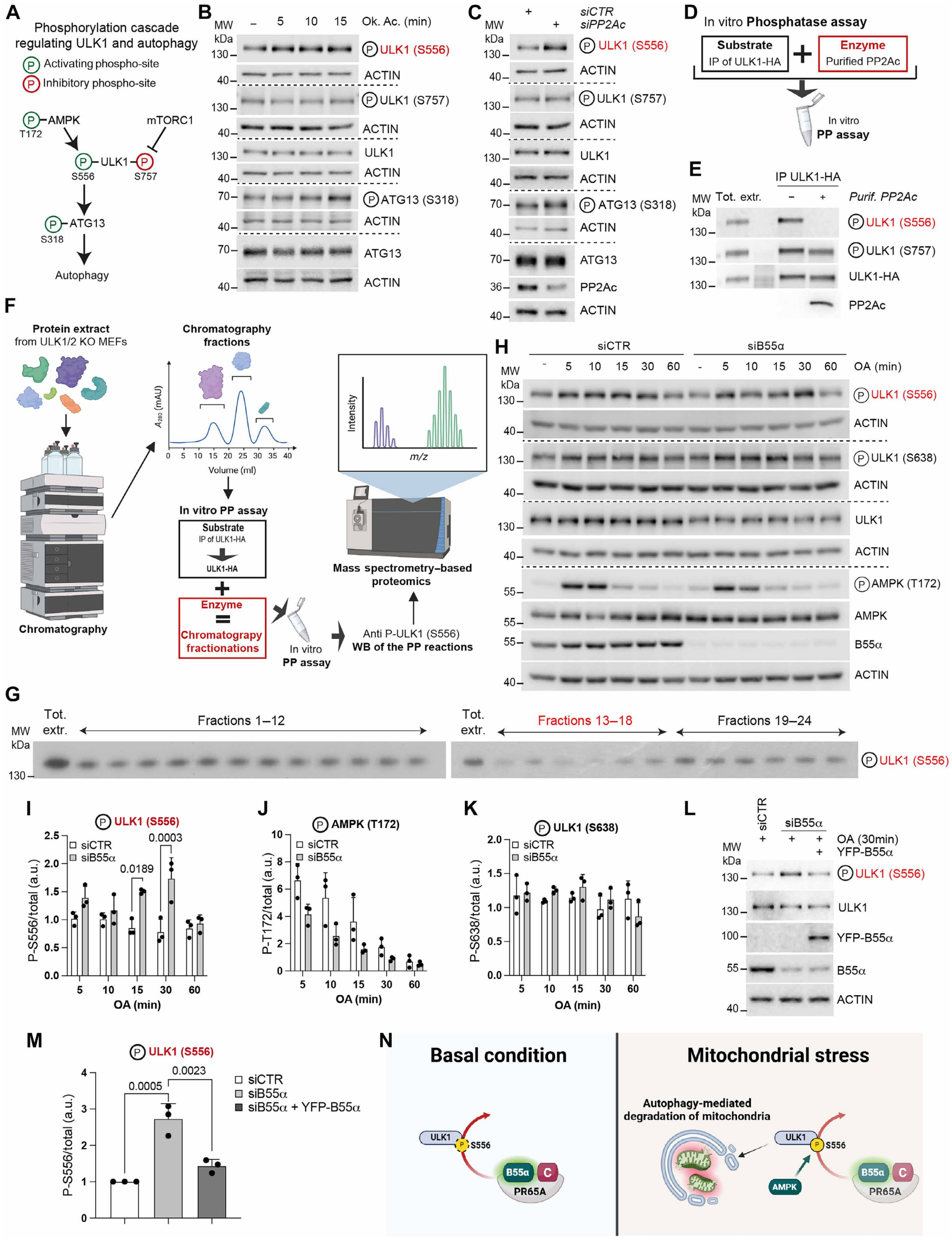

Fig. 1. PP2A-B55α dephosphorylates ULK1 at S556. (**A**) Phosphorylation events on ULK1, AMPK, and ATG13. (**B** and **C**) Protein extracts of HeLa cells treated with Ok. Ac. for 5 to 15 min (B) or depleted for PP2Ac (C) and immunoblotted for the indicated proteins. MW, molecular weight. (**D**) Schematic of the in vitro phosphatase (PP) assay. IP, immunoprecipitation. (**E**) In vitro phosphatase reactions obtained as in (D), negative control (–Purif. PP2Ac), and total protein extract of hemagglutinin (HA)–ULK1 immunoprecipitation were immunoblotted for the indicated proteins. Tot. extr., total extract. (**F**) Workflow of chromatography techniques coupled with liquid chromatography–mass spectrometry (LC-MS) proteomics to identify the protein phosphatase targeting P-ULK1 S556. Fractions from ULK1/2 double knockout (DKO) murine embryonic fibroblasts (MEFs) cell extracts, separated through chromatography, were tested for their phosphatase activity toward P-ULK1 S556 in an in vitro phosphatase assay. Active fractions were pooled and repurified through chromatography to further separate phosphatases of interest. Fractions from last chromatography column applied [1 to 24 in (G)] were analyzed by LC-MS proteomics. A_{280}, absorbance at 280 nm; *m/z*, mass/charge ratio; WB, Western blot. (**G**) In vitro phosphatase assays with fractions from the last chromatography column were immunoblotted for P-ULK1 S556. Active fractions (13 to 18) in red. (**H**) Cell extracts from oligomycin and antimycin A (OA)–treated Parkin-induced HeLa cells depleted for B55α were immunoblotted for the indicated proteins. (**I** to **K**) Quantification of the phosphorylated protein immunoblots represented in (H). a.u., arbitrary units. (**L**) Cell extracts from OA-treated HeLa cells stably expressing mCherry-Parkin, depleted for B55α, and induced for Yellow Fluorescent Protein (YFP)–B55α or not were immunoblotted for the indicated proteins. (**M**) Quantification of the phosphorylated protein immunoblots represented in (L). (**N**) PP2A-B55α–mediated regulation of P-ULK1 S556. Red and green arrows indicate inhibition and activation, respectively. ACTIN: Loading control for all immunoblots. Columns represent the mean ± SD relative to the corresponding untreated [–; in (I) to (K)] or control [siCTR; in (M)] sample. Two-way [(I) to (K)] or one-way (M) analysis of variance (ANOVA), and Tukey's multiple comparison test. Significant *P* values are reported in the figure.

are ubiquitin chains phosphorylated at S65 (P-Ubiq. S65), and the main receptors involved are optineurin (OPTN), NDP52 (CALCOCO2), and p62 (SQSTM1) (*29*, *30*). Because ULK1 activation is among the principal drivers of targeted autophagosome biogenesis, and we found it to be regulated by PP2A-B55α (Fig. 1), we examined whether also mitochondria priming for degradation was affected by down-regulating the phosphatase B55α. We thus performed RNA interference experiments in HeLa cells induced for Parkin expression and in SH-SY5Y cells differentiated through retinoic acid (RA) (*31*) and found increased levels of P-Ubiq. S65 in B55α-depleted total extracts from both models (Fig. 2, A and B, and fig. S2, A to F). Exogenous expression of YFP-B55α reversed the increase in P-Ubiq. S65 caused by B55α depletion, returning phosphorylation to control (siCTR + OA) conditions (Fig. 2, C and D). In addition, we analyzed the levels of both P-Ubiq. S65 and the main mitophagy receptors in mitochondria-enriched cellular fractions (Fig. 2, E to H). These experiments showed an increase in all positive regulators of mitophagy that we assessed, suggesting an inhibitory effect of PP2A-B55α on mitochondria priming toward dismissal. However, other early events of mitophagy remain unaffected. In particular, we did not find any difference in mitochondrial depolarization with or without B55α, neither under basal conditions nor upon OA treatment (fig. S3, A to D), thus uncoupling mitochondria priming from mitochondrial membrane charge. In line with these results, the levels of the Ser/Thr protein kinase PINK1 and the E3 ubiquitin ligase Parkin, which both accumulate on damaged mitochondria, are comparable between control and B55α-depleted cells (fig. S3, E to H). Notably, irrespective of the unchanged levels of the kinase PINK1 in B55α-depleted cells, increased P-Ubiq. S65 (Fig. 2, A to F) may be explained by B55α-mediated regulation of PINK1 activity, rather than total protein levels, through the hexokinase 2 (HK2)-induced assembly of an active high–molecular weight complex (*32*). Because TBK1 activity is required for efficient recruitment of OPTN and NDP52 to the ubiquitinated mitochondria (*33*), and we found both receptors enriched in mitochondria from B55α-depleted cells, we assessed whether B55α affects the activation of the mitophagy kinase TBK1. Similarly to PINK1, also in this case, we did not find any relevant effects (fig. S3, I and J). In sum, we show that B55α constrains mitochondria priming for recognition by the autophagy machinery by affecting P-Ubiq. S65 and mitophagy receptors, irrespective of the unchanged levels of mitophagy upstream kinases PINK1 and TBK1.

PP2A-B55α, while limiting early mitophagy signaling, is required for the subsequent Parkin-dependent mitochondrial clearance

ULK1 early activation, which is also achieved through S556 phosphorylation, is a crucial event in Parkin-dependent mitophagy. Because PP2A-B55α dephosphorylates ULK1 at S556 (Fig. 1), we tested its impact on later mitophagy execution by assessing mitochondrial content upon OA treatment in B55α knocked-down cells. Unexpectedly, B55α depletion impaired the degradation of the mitochondrial protein cytochrome C oxidase subunit II (COXII), which is encoded by mitochondrial DNA (mtDNA) (Fig. 3, A and B), and this phenotype was reverted by exogenous expression of YFP-B55α in B55α knocked-down cells (fig. S4, A and B). Next, we examined mitophagy using flow cytometry analysis of the exogenous reporter mKeima targeted to the internal mitochondrial membrane [(mt-mKeima (*34*, *35*)]. The excitation spectrum of mKeima shifts when exposed to low pH, allowing to measure the delivery of mitochondria into lysosomes as a readout of mitophagy. We validated the established reporter cell line by functional and subcellular localization assays (fig. S4, C to E). Consistent with the decreased degradation of COXII (Fig. 3, A and B), the B55α-depleted cells could not induce mitophagy to the same degree as control cells (Fig. 3C). We also confirmed this observation using an exogenous mitophagy sensor that is based on the tandem construct mCherry-GFP-FIS1, which is anchored to the external mitochondrial membrane (*36*). Because the GFP moiety is acid sensitive and mCherry is not, the fusion protein undergoes a change in the molecular weight once mitochondria are delivered to lysosomes through mitophagy (Fig. 3D). Thus, we assessed mitophagy induction by monitoring the ratio between mCherry (~25 kDa) and mCherry-GFP-FIS1 (~60 kDa) by immunoblotting, using an antibody against red fluorescent protein (RFP)/mCherry (Fig. 3, E to G). Consistent with the decreased degradation of COXII, B55α deficiency also prevented the delivery of the mitochondria to the lysosomes upon OA treatment, as shown by the exogenous reporters. Notably, an impairment of the mitophagy flux was also observed in undifferentiated and RA-differentiated SH-SY5Y cells, even in the absence of mitochondrial stress induced by drugs (fig. S5, A to C).

Next, to test whether the mitophagy impairment in B55α-depleted cells was due to defective autophagy, we measured autophagy induction upon OA treatment. As shown by both Western blot analysis of LC3BII levels and the autophagy flux assay, B55α is necessary to fully induce autophagy upon mitochondrial damage (Fig. 3, H to K, and fig. S6, A and B). Consistently, the rescue of B55α levels through the exogenous expression of YFP-B55α restored autophagy induction upon OA (fig. S6, C and D). In line with these results, the overall number of autophagosomes was strongly decreased by B55α knockdown upon OA treatment (Fig. 3, L and M), while their recruitment to damaged mitochondria was unaffected (fig. S6, E and F). Notably, B55α affected the autophagic flux, as well as mitophagy upon mitochondrial damage, in a Parkin-dependent manner (fig. S6, G and H). The lack of mitochondrial clearance in B55α-depleted cells resulted in cell death (fig. S6, I to K). Because B55α was previously reported to promote starvation-induced autophagy by counteracting mTORC1 activity toward an inhibitory phospho-site of ULK1 (S757) (*21*), we examined whether B55α does the same during mitophagy. However, as shown by mTORC1 autophosphorylation and phospho-ULK1 S757, neither mTOR activity nor P-ULK1 S757 was affected by B55α interference (fig. S7, A to C).

Together, these results support a role for B55α in the execution of the autophagy-mediated degradation of damaged mitochondria in Parkin-competent models.

PP2A-B55α activates TFEB upon mitochondrial damage to support Parkin-dependent mitophagy

Because of the apparent contradiction between the role of B55α in mitochondria priming for mitophagy and mitophagy execution, we set to investigate additional B55α targets responsible for the latter, besides ULK1. MiT/TFE transcription factor family members, among which Transcription Factor EB (TFEB) is the best characterized, are required for the efficient clearance of damaged mitochondria in Parkin-competent models (*37*). The mechanism underlying TFEB activation during mitophagy is distinct from the one induced by starvation/mTOR inhibition. While both mechanisms involve TFEB dephosphorylation and nuclear translocation, the protein phosphatase that targets TFEB during mitophagy remains unknown, as does

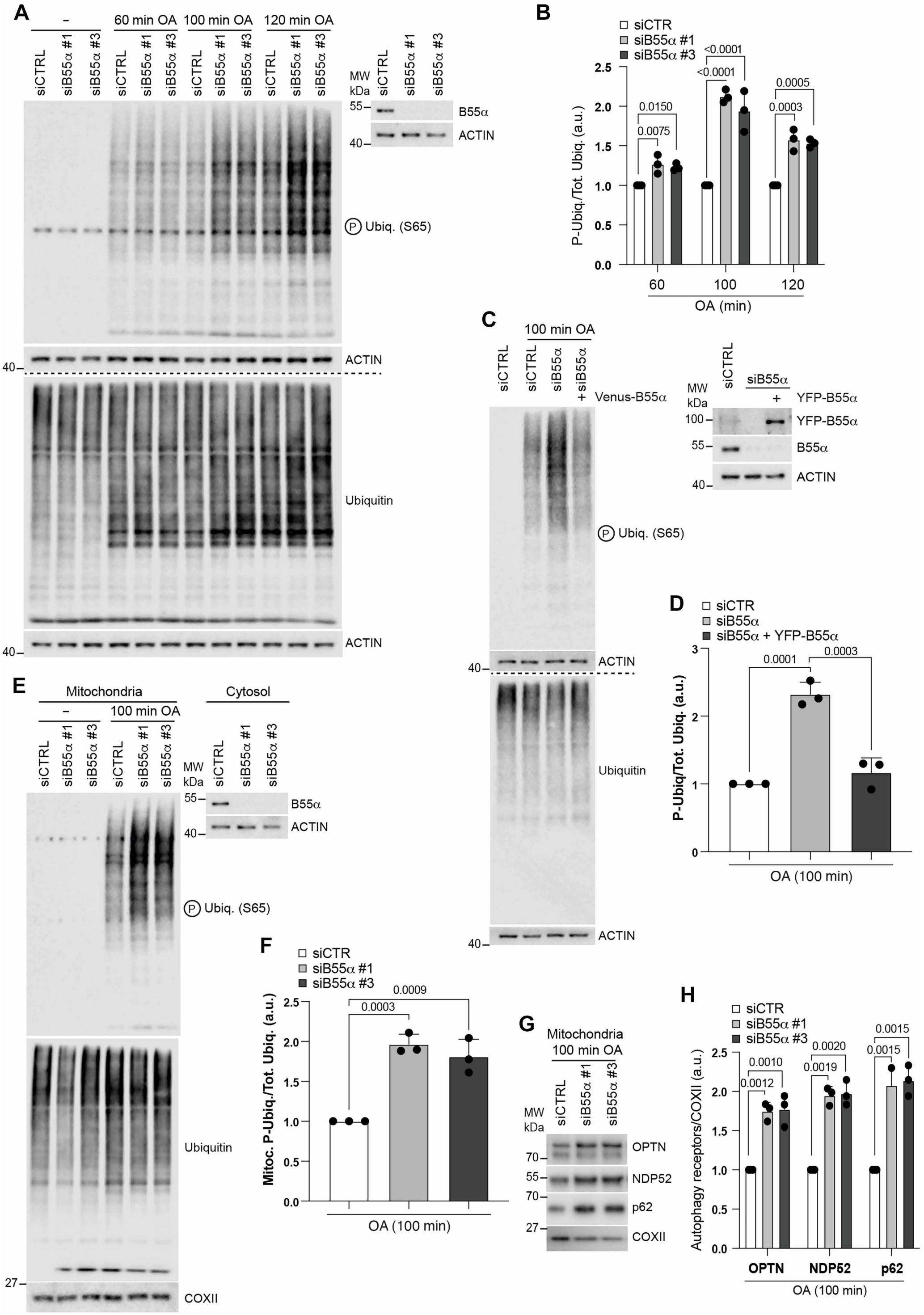

Fig. 2. PP2A-B55α inhibits mitochondria priming for recognition by the autophagy machinery. Cell extracts from Parkin-induced HeLa cells depleted for B55α or transfected with a nontargeting control oligo (siCTR) and treated with OA for the indicated time points were immunoblotted for the indicated proteins. ACTIN: Loading control. (**B**) Quantification of P-Ubiq. (S65) represented in (**A**). (**C**) Cell extracts from OA-treated HeLa cells stably expressing mCherry-Parkin, depleted for B55α or transfected with a nontargeting control oligo (siCTR), and induced for YFP-B55α or not were immunoblotted for the indicated proteins. ACTIN: Loading control. (**D**) Quantification of P-Ubiq. (S65) represented in (C). (**E**) Cytosol- and mitochondria-enriched fractions from cells as in (A), treated with OA for 100 min, and immunoblotted for the indicated proteins. ACTIN and cytochrome C oxidase subunit II (COXII): Loading controls. (**F**) Quantification of P-Ubiq. (S65) represented in (E). Mitoc., mitochondrial. (**G**) Mitochondria-enriched fractions from cells as in (A), treated with OA for 100 min, and immunoblotted for the indicated proteins. COXII: Loading control. (**H**) Quantification of OPTN, NDP52, and p62 represented in (G). All columns in the figure represent the mean ± SD of each time point relative to the corresponding control sample (siCTR). *P* values were calculated by one-way ANOVA, followed by Dunnett's multiple comparison test. Significant *P* values are reported in the figure.

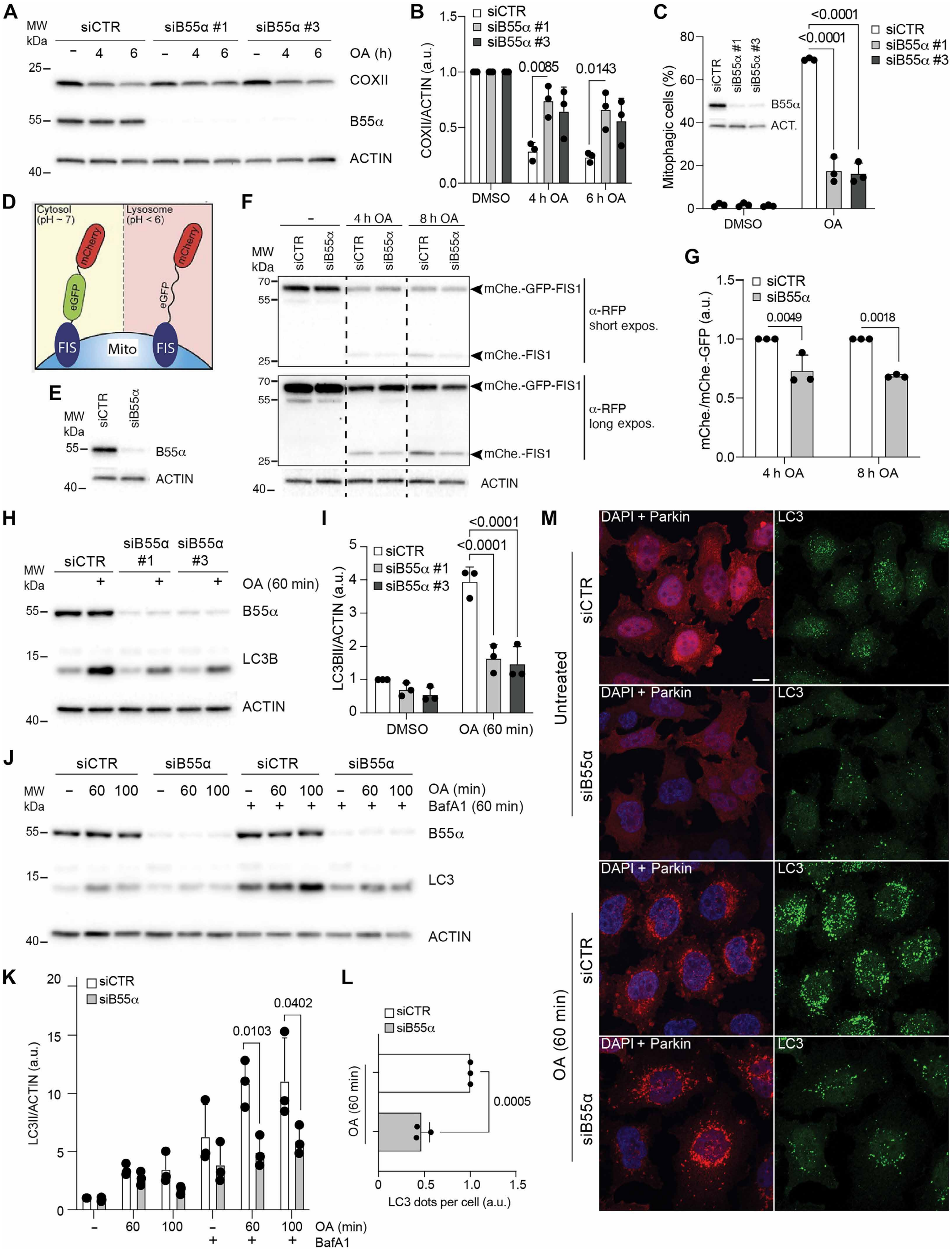

Fig. 3. PP2A-B55α, which limits early mitophagy signaling, is required for the subsequent Parkin-dependent mitochondrial clearance. (**A**) Cell extracts from Parkin-induced HeLa cells depleted for B55α and treated with OA were immunoblotted for the indicated proteins. h, hours. (**B**) Quantification of COXII represented in (A). (**C**)mt-mKeima flux analyzed by flow cytometry in OA-treated Parkin-induced HeLa cells depleted for B55α. Cell extracts from untreated cells were immunoblotted for the indicated proteins. Columns represent the mean ± SD. ACT., ACTIN. (**D**) Mitophagy reporter mCherry-GFP-FIS labeling cytosolic and lysosomal mitochondria in yellow and red, respectively. eGFP, enhanced GFP. (**E**) Cell extracts from untreated cells from (F) immunoblotted for the indicated proteins. (**F**) mCherry-GFP-FIS flux analyzed by immunoblot in OA-treated Parkin-induced HeLa cells depleted for B55α. Cell extracts were immunoblotted for the indicated proteins. mChe., mCherry; expos., exposure. (**G**) Quantification of mCherry-FIS1/mCherry-GFP-FIS1 ratio represented in (F). (**H**) Cells as in (A) were treated with OA for 60 min and immunoblotted for the indicated proteins. (**I**) Quantification of LC3B lipidation (LC3BII) represented in (H). (**J**) Cells as in (A) were treated with OA alone or in combination with Bafilomycin A (BafA1) for evaluation of autophagy flux by immunoblotting of LC3B. (**K**) Quantification of LC3BII represented in (J). (**L**) Quantification of the number of LC3B dots (in green) per cell, as seen in (**M**). Cells as in (A) were treated with OA for 60 min and stained for LC3B, Parkin, and Hoechst 33342 ($n = 3$ independent experiments, with 100 counted cells per experiment). ACTIN: Loading control for all immunoblots. All columns in the figure but in (C) represent the mean ± SD relative to the corresponding control sample. *P* values were calculated by two-way ANOVA, followed by Tukey's multiple comparison test in (B); one-way ANOVA, followed by Dunnett's multiple comparison test in (C), (I), and (K); and unpaired Student's *t* test (two-tailed) in (G) and (L). Significant *P* values are reported in the figure.

the identity of the TFEB phospho-sites that become dephosphorylated in this process (*37*). Because PP2A dephosphorylates and activates TFEB/TFE3 in response to oxidative stress induced by sodium arsenite (*38*), we wondered whether PP2A-B55α played the same role upon mitochondrial damage. Notably, TFEB and TFE3 are the most abundant MiT/TFEs in our used cell lines [www.proteinatlas.org (*39*)] and were thus chosen as representative members of the MiT/TFE family.

First, we tested whether the phosphorylation status of TFEB/TFE3 was altered by B55α inhibition, by monitoring TFEB/TFE3 migration patterns during SDS-PAGE by immunoblotting (*40*). We collected protein samples upon B55α depletion and incubated them with or without the lambda phosphatase (λ-PP) (Fig. 4A). We found that TFEB/TFE3 migrate slower in the B55α-depleted samples compared to their control counterpart, most likely because of increased phosphorylation, which resulted in a shift that was abolished by λ-PP treatment. In line with its altered phosphorylation pattern, TFEB does not efficiently translocate to the nucleus in B55α-depleted cells treated with OA, compared to the relevant control (siCTR + OA) (Fig. 4, B to D). Although TFEB dephosphorylation and nuclear translocation upon mitochondrial damage were previously reported, the involved phospho-sites are not clear and require future investigation (*37*), at a variance with the well-characterized mTORC1-targeted and Extracellular signal–Regulated Kinase 2 (ERK2)–targeted sites (S142/211), which regulate TFEB translocation upon starvation (*41*–*44*). The fact that B55α does not affect mTORC1 activity (fig. S7, A to C) implies that B55α directly targets TFEB upon mitochondrial damage in an mTORC1-independent manner. In agreement with TFEB being a direct target of B55α, its OA-induced nuclear translocation is restored in B55α knockdown cells upon exogenous expression of YFP-B55α (fig. S8, A and B). Transcriptomic analysis followed by Gene Ontology enrichment analysis (GOEA), with the output restricted to cellular compartment (CC) terms, identified lysosome genes among those down-regulated by B55α silencing (Fig. 4E, blue). In addition, a manually curated analysis detected 1207 genes previously reported as TFEB targets (CLEAR-containing genes) to be also decreased upon B55α knockdown (Fig. 4E, green). In addition, in this case, the GOEA analysis found lysosome among the categories down-regulated by B55α silencing in the CLEAR-gene dataset. To validate these results, we compared the impact of B55α and TFEB status on autophagy induction upon OA and found that autophagy is decreased to a similar extent in B55α- and TFEB-depleted cells (Fig. 5, A to D). The expression of a constitutively nuclear TFEB (phospho-silencing mutant at the mTORC1/ERK2 target sites: S142/211A) rescued both autophagy and mitophagy defects induced by the B55α knockdown (Fig. 5, E to H). Together, these data establish also a role for B55α in TFEB activation and nuclear translocation upon mitochondrial damage to sustain the execution of Parkin-dependent mitophagy.

PP2A-B55α inhibits mitochondrial biogenesis

Because mitochondrial homeostasis is the result of mitophagy and mitochondrial biogenesis, we also investigated whether B55α participates in both these processes. First, we measured the mitochondrial mass in B55α-depleted cells by quantifying mtDNA through immunofluorescence and real-time quantitative polymerase chain reaction (qPCR) (Fig. 6, A to C). Both assays revealed an increased amount of mtDNA upon B55α knockdown and the rescue to control levels (siCTR) upon exogenous expression of YFP-B55α in B55α-depleted cells (Fig. 6D). Because of the proven role of B55α in promoting mitophagy (Fig. 3, A to G), the increase in the mitochondrial mass could result, in principle, from an accumulation of damaged mitochondria. However, we could not detect any relevant alterations in the mitochondrial pool of B55α-depleted cells, as shown by stable mitochondrial membrane potential and continued mitochondrial function (figs. S3, B and C, and S9, A to G). On the basis of these data, we hypothesized that mitochondrial biogenesis may also play a role in B55α-dependent mitochondrial number control. Consistent with this hypothesis, in B55α-depleted cells, we observed an increase in the expression of mitochondria-related gene categories in the transcriptomic analysis, followed by GOEA, with the output restricted to CC terms (Fig. 6E). This result suggested a transcriptional program downstream of B55α and relevant to the regulation of mitochondrial mass. By a manually curated analysis, we also found 20 genes associated with mitochondrial biogenesis processes as up-regulated upon B55α depletion (fig. S10). Overall, these results point toward a role for B55α in mitochondrial biogenesis and prompted us to assess the levels of two key regulators implicated in this process: PGC-1α and mitochondrial transcription factor A (TFAM), a nuclear transcriptional coactivator and a regulator of the abundance/transcription of mtDNA, respectively. We observed an increase in mRNA and both mRNA and protein levels for PGC-1α and TFAM, respectively, both in HeLa-Parkin and neuroblastoma cells knocked-down for B55α (Fig. 6, F to K). Notably, TFAM up-regulation, observed in B55α-depleted cells, was lost upon exogenous expression of YFP-B55α (Fig. 6, L and M). In addition, we also monitored the levels of the mitochondrial proteins COXIV and TIM23, as an indirect readout of the mitochondrial mass (Fig. 6, N and O). All these experiments showed an increase in mitochondrial mass following B55α knockdown.

Together, these results identify PP2A-B55α as a regulator of mitochondrial mass by also impinging on mitochondrial biogenesis pathways driven by PGC-1α.

PP2A-B55α regulates the Parkin substrate and PGC-1α inhibitor PARIS

Because we found that B55α (i) regulates Parkin-dependent mitochondria dismissal and (ii) impinges on the mitochondrial biogenesis regulator PGC-1α (Fig. 6 and fig. S10), we set up to investigate any potential functional cross-talking among the relevant factors critical during these processes. PGC-1α is inhibited by its interactor ZNF746 (PARIS), which has been reported to be also a direct substrate of Parkin (*45*). On the basis of these findings, we hypothesized that, upon B55α depletion, PARIS levels decrease in a Parkin-dependent manner, to drive a PGC-1α–mediated program of mitochondrial biogenesis.

First, we validated the ability of B55α to modulate PARIS levels in two Parkin-competent human cancer cell models, namely, SH-SY5Y and HeLa cells, induced for Parkin expression. In both models, B55α depletion resulted in decreased PARIS levels (Fig. 7, A to D). Next, we further confirmed that B55α depends on Parkin to regulate PARIS by comparing HeLa cells induced or not for Parkin expression. B55α knockdown resulted in decreased PARIS in Parkin-expressing cells only (Fig. 7, E and F). Last, we monitored PARIS protein half-life in Parkin-competent cells, depleted or not of B55α. In line with the hypothesis that B55α regulates PARIS through its E3 ligase Parkin, PARIS was less stable in B55α-depleted cells, most likely because of Parkin-mediated degradation (Fig. 7, G and H). In

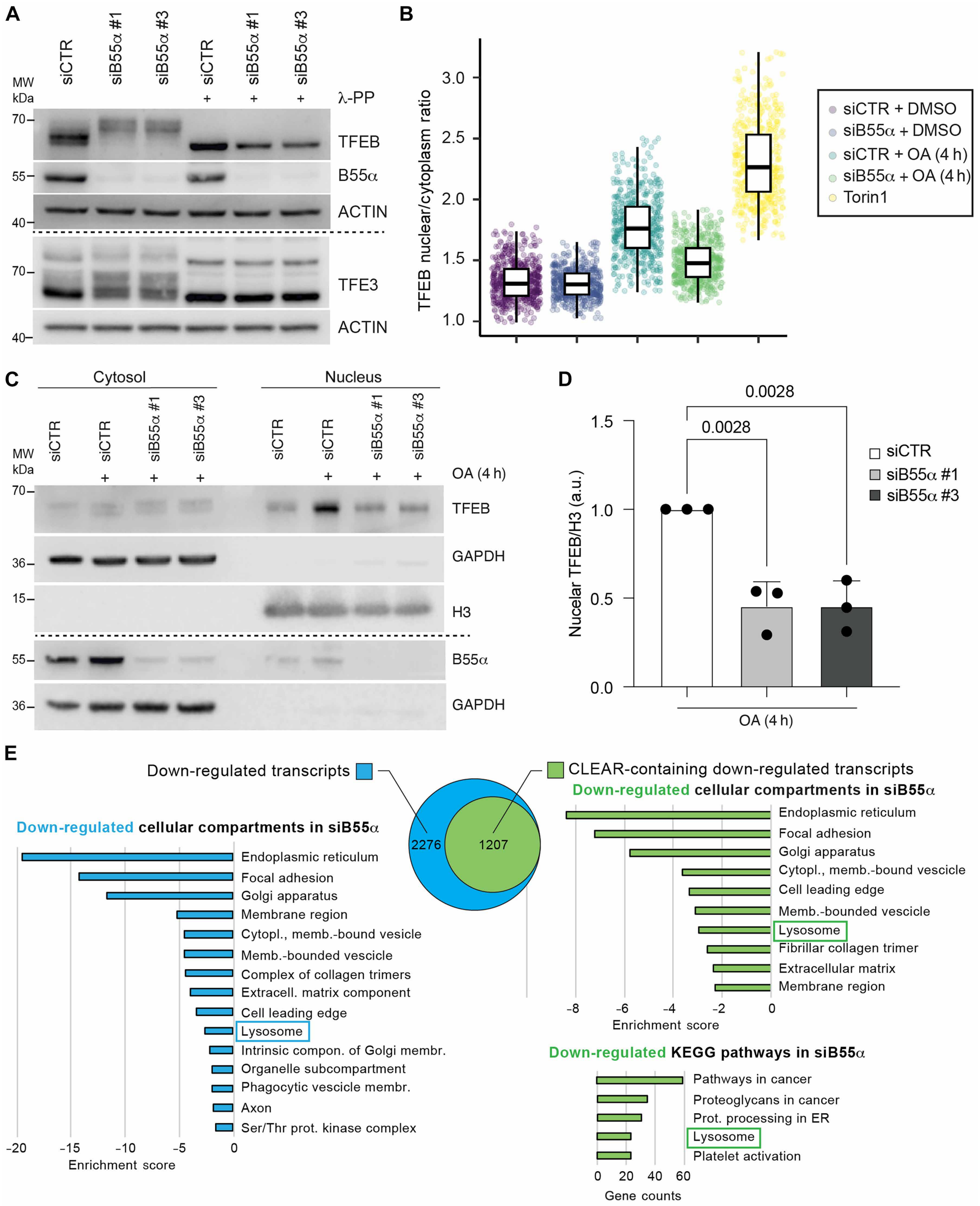

Fig. 4. PP2A-B55α activates TFEB upon mitochondrial damage to support Parkin-dependent mitophagy. (**A**) Cell extracts from Parkin-induced HeLa cells depleted for B55α or transfected with a non-targeting control oligo (siCTR) were incubated with the +λ-PP or the vehicle at 30°C for 30 min. Samples were immunoblotted for the indicated antibodies. ACTIN: Loading control. (**B**) Box plot of single-cell analysis for nuclear-to-cytoplasm ratio of cells as in (A), treated with OA for 4 hours or Torin1 for 1 hour. $n = 500$ from four biologically independent replicates. Data in box plot are presented as first quartile, median, and third quartile. (**C**) Protein extracts from nuclear and cytosolic fractions of cells as in (A) treated with OA for 4 hours were immunoblotted for the indicated antibodies. Glyceraldehyde-3-phosphate dehydrogenase (GAPDH) and histone 3 (H3) were used as cytosolic and nuclear markers, respectively, and as loading controls. (**D**) Quantification of nuclear TFEB represented in (C). Columns represent the mean ± SD relative to the corresponding control sample. *P* values were calculated by one-way ANOVA, followed by Tukey's multiple comparison test. Significant *P* values are reported in the figure. (**E**) All significant Cellular Compartments [(CC), left plot] in which the 2276 genes (of 4417) are negatively regulated are mainly enriched. Center: The Venn diagram shows that 1207 of 2276 genes are CLEAR-containing genes. Right plot: CC and Kyoto Encyclopedia of Genes and Genomes (KEGG) pathway enrichment of the 1207 CLEAR-containing genes. The enrichment score for each CC cluster is plotted, while for the KEGG pathways, the gene counts are plotted. Cytopl., cytoplasmic; memb.-bound, membrane-bound; Extracell., extracellular; prot., protein; ER, endoplasmic reticulum.

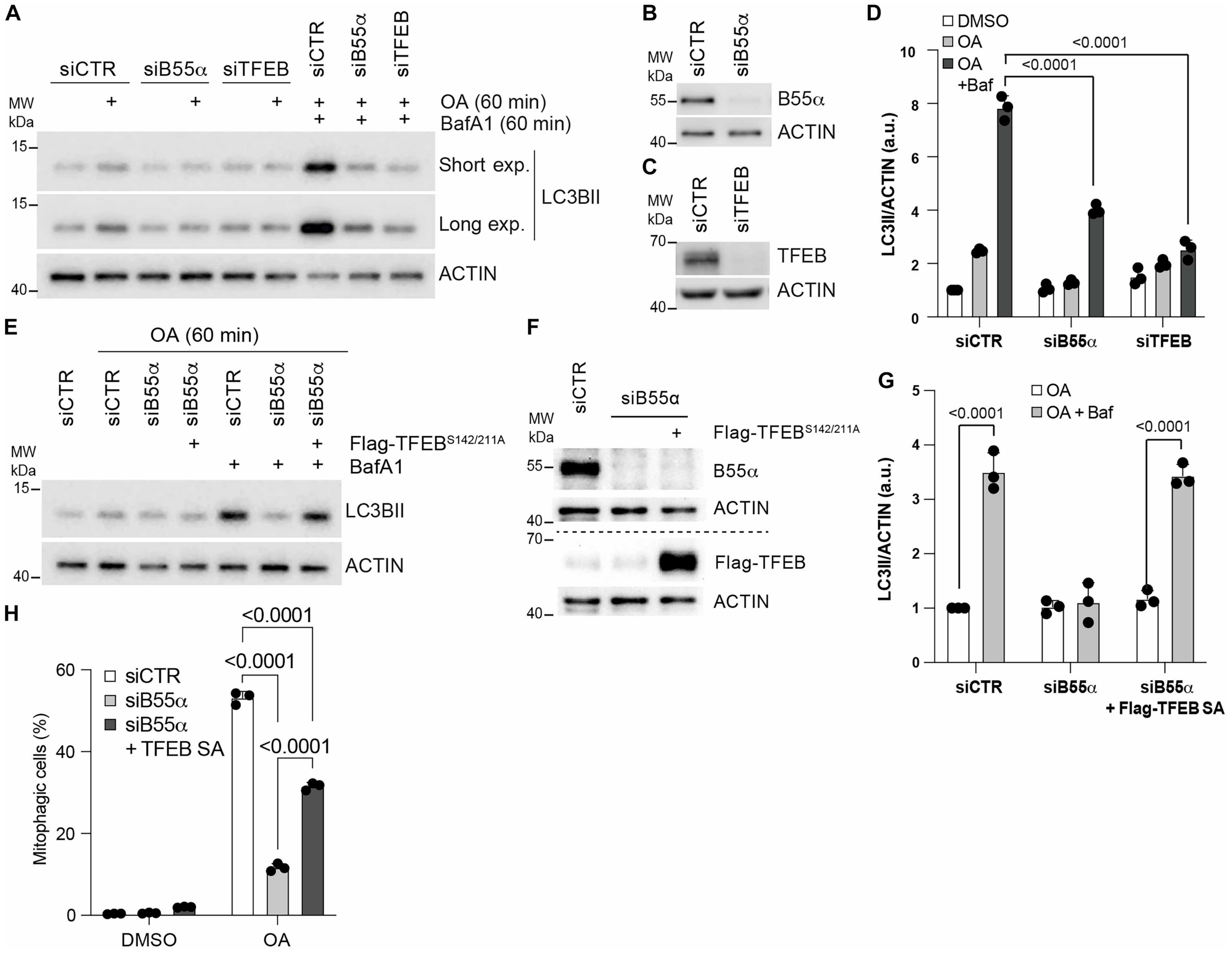

Fig. 5. PP2A-B55α–mediated regulation of mitophagy depends on TFEB. (**A**) Cell extracts from Parkin-induced HeLa cells depleted for B55α or TFEB or transfected with a non-targeting control oligo (siCTR), treated with OA, alone or combined with BafA1 for 60 min, were immunoblotted for the indicated proteins. ACTIN: Loading control. (**B** and **C**) Protein extracts from knocked-down untreated cells from (A) where immunoblotted for the indicated antibodies. ACTIN: Loading control. (**D**) Quantification of LC3BII represented in (A). Columns represent the mean ± SD relative to untreated control sample (siCTR). (**E**) Cell extracts from Parkin-induced HeLa cells depleted for B55α or transfected with a nontargeting control oligo (siCTR), transiently expressing Flag-TFEB (S142/211A), and treated with BafA1 for 60 min were immunoblotted for the indicated antibodies. ACTIN: Loading control. (**F**) Cell extracts from untreated cells as in (E) were immunoblotted for the indicated antibodies. ACTIN: Loading control. (**G**) Quantification of LC3BII represented in (E). Columns represent the mean ± SD relative to untreated control sample (siCTR). (**H**) Flow cytometry analysis of mt-mKeima flux in Parkin-induced HeLa cells stably expressing mt-mKeima, depleted for B55α or transfected with a nontargeting control oligo (siCTR), transiently transfected with Flag-TFEB (S142/211A), and treated with OA for 4 hours. Columns represent the mean ± SD. All *P* values in the figure were calculated by one-way ANOVA, followed by Dunnett's multiple comparison test. Significant *P* values are reported in the figure.

RA-differentiated SH-SY5Y cells, B55α depletion decreases and augments PARIS and TFAM protein levels, respectively (Fig. 7, I to K), in agreement with a role for B55α in mitochondrial biogenesis induction through PARIS in this model. Together, our results suggest that a PP2A-B55α-Parkin-PARIS axis regulates mitochondrial biogenesis.

PP2A-B55α rescues neurodegenerative phenotypes in flies in a Parkin-dependent manner

In the light of the multifaceted role of PP2A-B55α at the crossroad between mitochondrial biogenesis and Parkin-mediated mitophagy, we wondered whether this protein phosphatase could affect PINK1- and/or Parkin-related neurodegenerative phenotypes in vivo. To this end, we obtained flies knocked-down (KD) for the *Drosophila melanogaster* ortholog of the B55 family, *Tws*, and crossed them with either *Pink1* or *Parkin* knockout (KO) flies. As previously observed, the ultrastructural analysis of both *Pink1* and *Parkin KO* muscle samples revealed an accumulation of damaged mitochondria (Fig. 8, A and B; panels *Parkin KO* and *Pink1 KO*) (*46*, *47*), while *Tws KD* muscles are almost unaffected (Fig. 8, A and B; panels *Tws KD*). In *Pink1 KO::Tws KD* flies, we observed a striking rescue of the mitochondrial phenotype (Fig. 8A; *Pink1 KO::Tws KD* panel), at variance with the *Parkin KO::Tws KD* flies, which showed an even more severe disruption of the muscle ultrastructure when compared

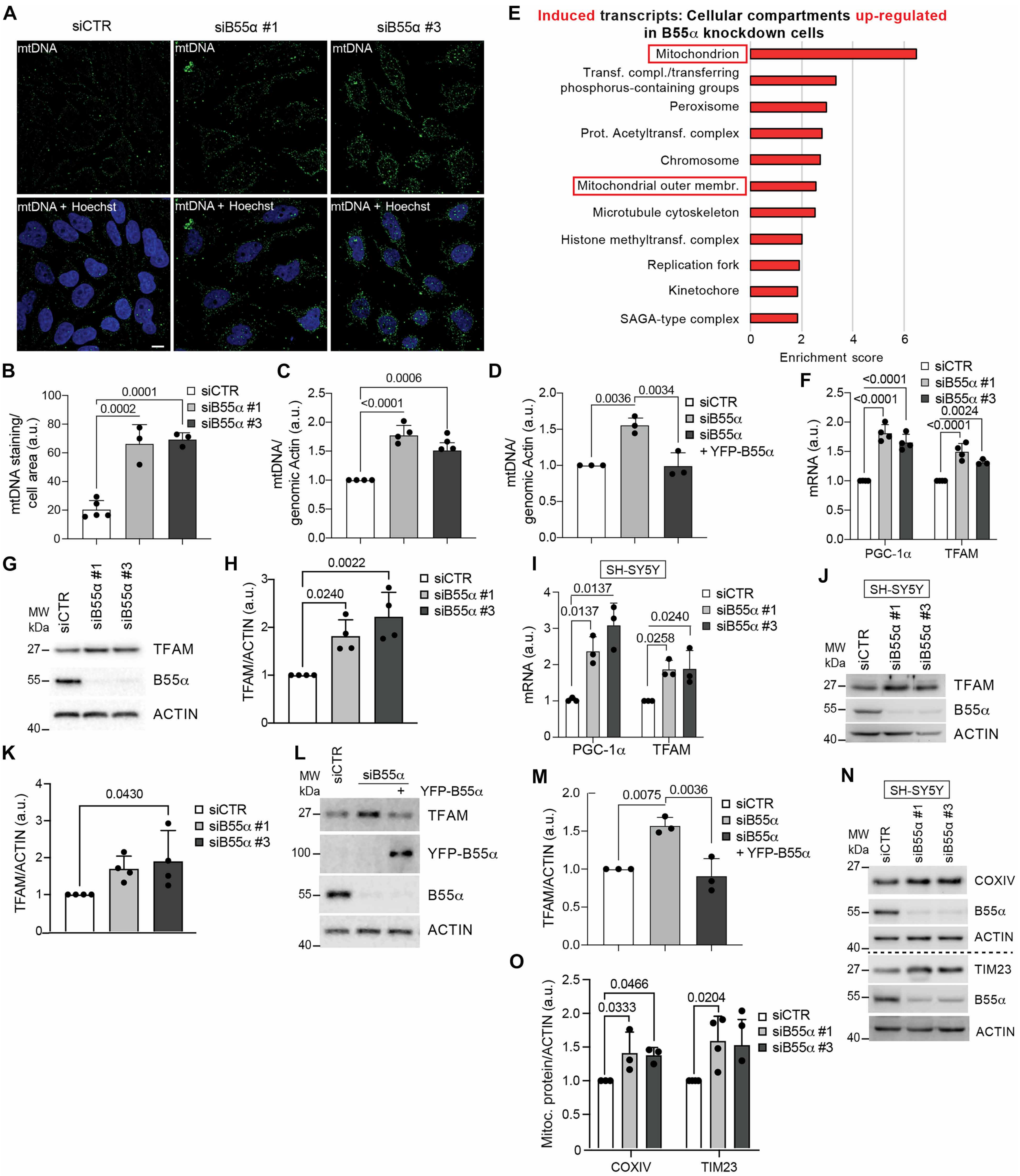

Fig. 6. PP2A-B55α inhibits mitochondrial biogenesis. (**A**) Parkin-induced HeLa cells depleted for B55α were stained for mtDNA and Hoechst 33342. (**B**) Quantification of mtDNA/cell area ratio for cells as seen in (A). (**C**) Reverse transcription qPCR (RT-qPCR) analysis of mtDNA copy number for cells as in (A). (**D**) RT-qPCR analysis of mtDNA copy number for HeLa cells stably expressing mCherry-Parkin, depleted for B55α, and induced for YFP-B55α or not. (**E**) All significant CC in which the 2141 genes (of 4417) are positively regulated are mainly enriched. Transf. compl., transfer complex; acetyltransf., acetyltransferase; methyltransf., methyltransfase. (**F**) RT-qPCR analyses of PGC-1α and TFAM mRNA in cells as in (A). (**G**) Protein extracts from cells as in (A) were immunoblotted for the indicated antibodies. (**H**) Quantification of TFAM represented in (G). (**I**) RT-qPCR analyses of PGC-1α and TFAM mRNA in SH-SY5Y cells depleted for B55α. (**J**) Protein extracts from cells as in (I) were immunoblotted for the indicated proteins. (**K**) Quantification of TFAM represented in (J). (**L**) Cell extracts from cells as in (D) were immunoblotted for the indicated proteins. (**M**) Quantification of TFAM represented in (L). (**N**) Protein extracts from cells as in (I) were immunoblotted for the indicated proteins. (**O**) Quantification of mitochondrial proteins represented in (N). ACTIN: Loading control for all immunoblots. Columns represent the mean ± SD [in (B), (H), (K), (M), and (O)] or the mean ± SEM [in (C), (D), (F), and (I)]. All *P* values were calculated by one-way ANOVA, followed by Dunnett's multiple comparison test. Significant *P* values are reported in the figure.

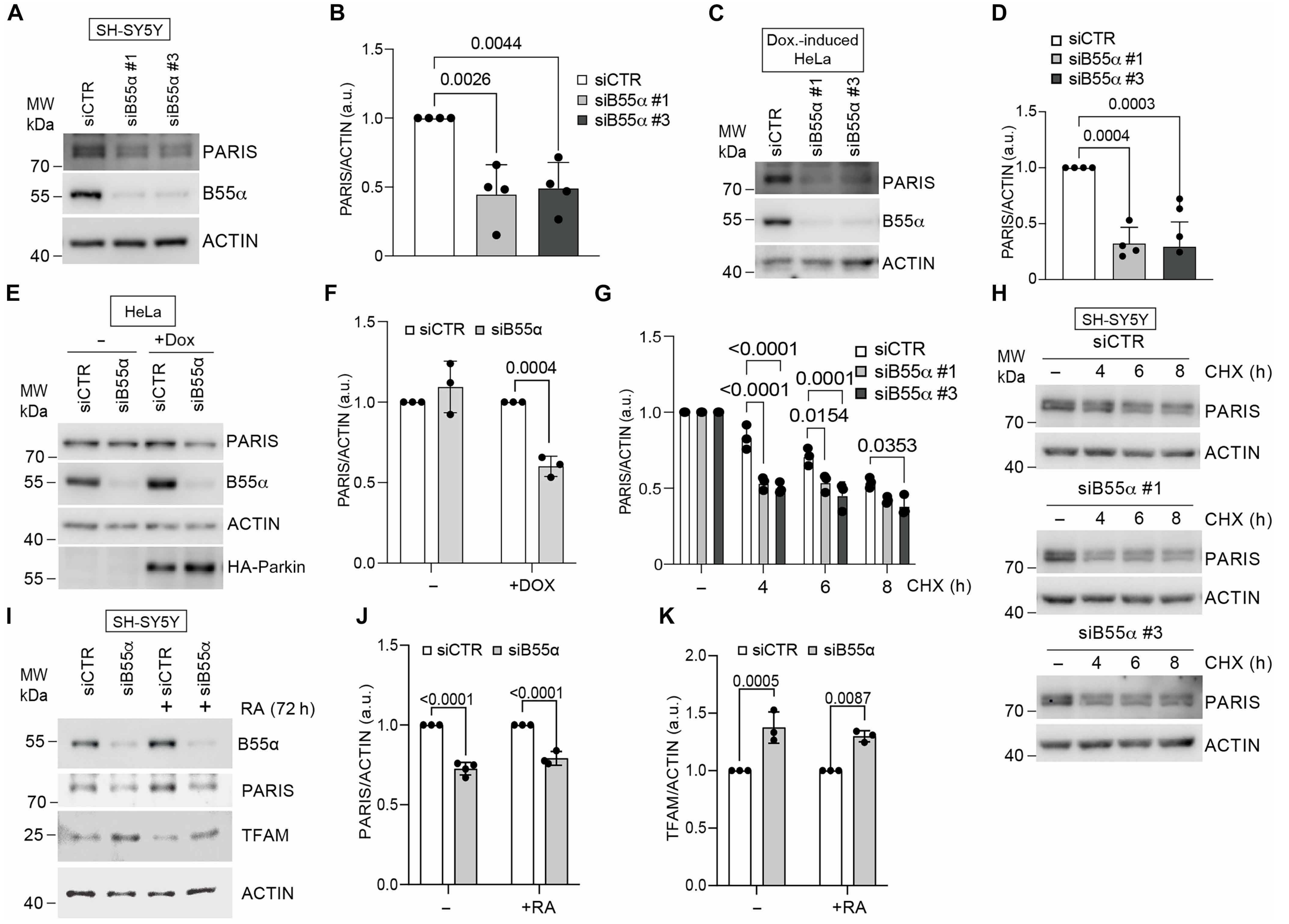

Fig. 7. PP2A-B55α regulates the Parkin substrate and PGC-1α inhibitor PARIS. (**A**) Protein extracts from SH-SY5Y cells depleted for B55α were immunoblotted for the indicated antibodies. (**B**) Quantification of PARIS represented in (A). (**C**) Protein extracts from Parkin-induced HeLa cells depleted for B55α were immunoblotted for the indicated antibodies. (**D**) Quantification of PARIS represented in (C). (**E**) Protein extracts from HeLa cells depleted for B55α, and induced or not for Parkin expression (+/− Dox: doxycycline), were immunoblotted for the indicated proteins. (**F**) Quantification of PARIS represented in (E). (**G** and **H**) Protein extracts from cells as in (A), treated with cycloheximide (CHX) for the indicated time points, were immunoblotted for the indicated proteins. In (G), quantification of PARIS represented in (H). (**I**) Cell extracts from SH-SY5Y cells depleted for B55α, and treated with RA for 72 hours, were immunoblotted for the indicated antibodies. (**J**) Quantification of PARIS represented in (I). (**K**) Quantification of TFAM represented in (I). ACTIN: Loading control for all immunoblots. Columns represent the mean ± SD. *P* values were calculated by one-way ANOVA in (B) and (D) or two-way ANOVA in (G), followed by Tukey's multiple comparison test, or unpaired Student's *t* test (two-tailed) in (F), (J), and (K). Significant *P* values are reported in the figure.

with the single *Parkin KO* (Fig. 8B; *Parkin KO::Tws KD* panel). In addition, we monitored the climbing defects affecting *Pink1 KO*, *Parkin KO*, or the double *Pink1 KO::Tws KD* and *Parkin KO::Tws KD* flies, and we obtained results in line with the morphological ultrastructural defects, with *Tws KD* partially rescuing the climbing defects in *Pink1 KO* but not in *Parkin KO* (Fig. 8, C and D). Our results showed that B55α promotes mitophagy in Parkin-competent mammalian cells (Fig. 3); therefore, we expect the lack of *Tws* to impair mitophagy in both *Pink1* and *Parkin KO* flies, which already have mitochondrial defects. However, because B55α depletion also induces mitochondrial biogenesis in mammalian cells (Fig. 6), we foresee an increase in the mitochondrial biogenesis in *Tws*-depleted models in a Parkin-dependent manner, similarly to the mammalian counterpart. This mechanistic interpretation may explain why *Tws KD* rescues neurodegenerative phenotypes in *Pink1 KO* animals but not in *Parkin KO* ones. The improvement in mitochondrial and climbing phenotypes observed in *Pink1 KO::Tws KD* is likely due to an increase in mitochondrial biogenesis, which partially compensates for damaged mitochondria, while the absence of Parkin may prevent compensation of the mitochondrial biogenesis mediated by the PP2A-B55α-Parkin-PARIS axis (fig. S11A). Together, these results suggest that PP2A-B55α–mediated regulation of mitochondrial biogenesis may also be relevant in vivo in neurodegenerative models, thereby identifying B55α as a potential therapeutic target in a relevant subset of neurodegenerative diseases.

DISCUSSION

Owing to its reversible and highly dynamic nature, protein (de) phosphorylation is commonly involved in the regulation of cellular

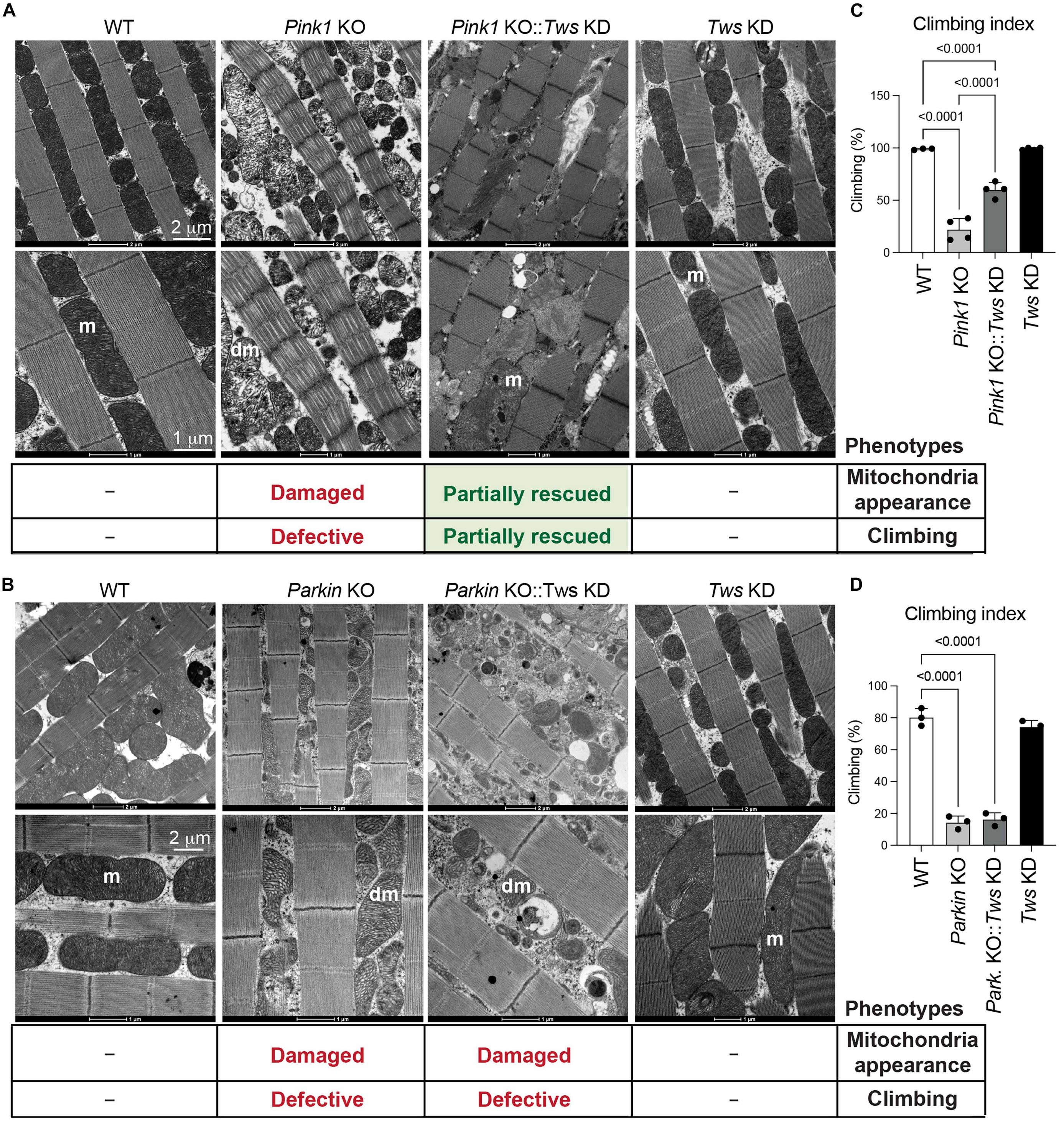

Fig. 8. PP2A-B55α rescues neurodegenerative phenotypes in flies in a Parkin-dependent manner. (**A** and **B**) Ultrastructural analysis of the indirect flight muscles and mitochondria from fly thoraces of the indicated genotypes. (**C**) Graph bar shows mean ± SEM of the percentage of climbing flies of the indicated genotype from at least three independent experiments. *P* values were calculated by one-way ANOVA, followed by Tukey's multiple comparison test. Significant *P* values are reported in the figure; *n* = 3. (**D**) Graph bar shows mean ± SEM of the percentage of climbing flies of the indicated genotype from at least three independent experiments. *P* values were calculated by one-way ANOVA, followed by Tukey's multiple comparison test. Significant *P* values are reported in the figure; *n* = 3 to 4. m, mitochondria; dm, damaged mitochondria. Complete genotypes: Actin-GAL4/+ (WT); Actin-GAL4/+; park25/park25 (Parkin KO); Actin-GAL4/UAS-Tws-RNAi; park25/park25 (Park. KO::Tws KD); Pink1B9/Y; Actin-GAL4/+ (Pink1 KO); Pink1B9/Y; Actin-GAL4/UAS-Tws-RNAi (Pink KO::Tws KD); and Actin-GAL4/UAS-Tws-RNAi (Tws KD).

homeostatic processes controlled by internal and external cues. In this context, the coordinated activity of protein kinases and phosphatases is the key, although phosphatases are often less well characterized. Here, we identify the protein phosphatase PP2A-B55α as a shared regulator of the processes of mitochondrial turnover and biogenesis and therefore a key controller of mitochondrial number. Notably, PP2A-B55α impinges on both upstream and downstream regulation of mitophagy in a time-dependent manner. In addition, both these emerging roles of PP2A-B55α that we report here, in mitochondrial turnover and biogenesis, respectively, rely on the mitophagy E3 ligase Parkin (fig. S11B). Last, we show that PP2A-B55α depletion partially rescues neurodegenerative phenotypes in vivo in *D. melanogaster*.

Parkin-mediated mitophagy depends on both early regulatory events, occurring minutes after mitochondrial damage (e.g., ULK1 phosphorylation and "eat me" signals) (*16*, *19*, *29*, *30*) and later events occurring several hours after induction (e.g., TFEB-mediated transcription of autophagy genes) (*37*). While the former events ensure prompt mitophagy induction, the latter sustain prolonged autophagy execution for mitochondrial degradation. We found that both early and late phases of mitophagy are affected by PP2A-B55α. In particular, PP2A-B55α–mediated dephosphorylation of ULK1 contributes to this kinase activation within 15 to 30 min and provides the "eat me" signal accumulation on mitochondria (Figs. 1 and 2), while 2 to 4 hours after mitophagy induction, an increased PP2A-B55α activity on TFEB promotes the nuclear translocation of this transcription factor (Fig. 4). Therefore, PP2A-B55α targeting of specific regulators changes between steady state and mitophagy induction, as well as with mitophagy timing. This scenario resembles the timely and ordered regulation of cell division events by a number of protein phosphatases, including PP2A-B55α (*48*). Hence, it would be interesting to find out whether the endogenous inhibitors that temporally regulate B55α in the cell cycle (e.g., ARPP19/ENSA and FAM122A) have a similar role during mitophagy (*49*, *50*). Another possibility of functionally modulating this process is the intervention of scaffold proteins, temporally protecting PP2A-B55α targets from the phosphatase. In the case of TFEB, it is tempting to speculate that the 14-3-3 proteins interacting with TFEB may prevent B55α-mediated dephosphorylation at early time points of mitophagy, as they do in the presence of nutrients to avoid calcineurin-mediated TFEB dephosphorylation, which instead is induced upon starvation (*51*).

Because both ULK1 phosphorylation at S556 (P-ULK1 S556) and TFEB activation occur during exercise-induced mitophagy (*18*, *52*), it is plausible that B55α-mediated regulation of these targets is also relevant in such a physiological context.

Our findings reveal that B55α influences mitochondrial turnover also in RA-differentiated SH-SY5Y cells, even in the absence of mitochondrial stress induced by drugs. This suggests a previously uncharacterized role for B55α in regulating basal mitophagy for maintaining neuronal homeostasis. In addition, B55α may help shape mitochondrial populations to meet the specific metabolic demands and unique biological characteristics of neurons (*33*, *53*).

Besides its role in mitophagy, here, we describe a previously unappreciated role for PP2A-B55α in mitochondrial biogenesis through an interplay with the mitophagy E3 ligase Parkin. While sustaining mitophagy induction upon mitochondrial damage, PP2A-B55α inhibits mitochondrial biogenesis under steady-state conditions through a Parkin-PARIS-PGC-1α axis. Notably, because phosphorylation at S322/613 primes PARIS for Parkin-mediated degradation (*54*), PP2A-B55α may contribute to the regulation of PARIS stability by affecting its phosphorylation. Consistent with this hypothesis, depletion of fly B55 (*Tws*) rescues both the climbing defects of the flies and their mitochondria ultrastructural defects in the *Pink1* KO *D. melanogaster* model, while failing to do the same in Parkin KO counterpart flies (Fig. 8), suggesting that the observed phenotypic rescue may depend on the induction of mitochondrial biogenesis through the Parkin-PARIS axis (fig. S11A). This hypothesis is also supported by the capability of PARIS depletion to rescue both *Pink1* and *Parkin* KO defects in *D. melanogaster* by promoting mitochondrial biogenesis while leaving mitophagy unaffected (*55*). These findings indicate that PP2A-B55α–mediated regulation of mitochondrial homeostasis may also be relevant to some additional human neurodegenerative disorders characterized by unbalanced mitophagy and mitochondrial biogenesis, such as mitochondrial myopathies and Duchenne's muscular dystrophy (*56*, *57*), further highlighting the potential importance of our current findings for biomedicine.

MATERIALS AND METHODS

A full list of the reagents used, including RRIDs, is also reported in table S2.

Cell culture

Human Embryonic Kidney 293T (HEK293T), hemagglutinin (HA)–Parkin–inducible HeLa cells (gift from I. Dikic, Institute of Biochemistry II, Goethe University School of Medicine, Frankfurt, Germany) (*27*), YFP-B55α inducible HeLa cells (gift from J. Nilsson, Copenhagen University, Copenhagen, Denmark) (*58*), wild-type (WT)/DKO MEFs (gift from S. Tooze, The Francis Crick Institute, London, UK), and derived stable cell lines were cultured in Dulbecco's modified Eagle's medium (DMEM) high-glucose, GlutaMAX supplement (Gibco, 31966-021), supplemented with 10% fetal bovine serum (FBS; Gibco, 10270-106) and 1% penicillin/streptomycin (P/S; Gibco, 15140-122). SH-SY5Y cells were cultured in DMEM/F-12 GlutaMAX supplement (Gibco, 31331-028), supplemented as specified for DMEM above, and maintained in a humidified atmosphere containing 5% CO_2 at 37°C. All cell lines used in the present study were tested negative for mycoplasma contamination at least every 3 months. Commercially available cell lines were purchased from American Type Culture Collection and validated by the company by short tandem repeat analysis. SH-SY5Y differentiation was induced by 10 μM RA (Sigma-Aldrich, R2625) in DMEM/F12 supplemented with 1% FBS for 72 hours (*31*) and in cells depleted for B55α (pooled siB55α #1 and #3) or transfected with a nontargeting control oligo (siCTR), as described below. Morphological evaluation of neurite projections and Western blot analysis of N-MYC and p21 were used for the assessment of differentiation. To induce HA-Parkin expression in HeLa cells and YFP-B55α in mCherry-Parkin HeLa cells, cells were incubated overnight or for 48 hours with doxycycline (0.5 μg/ml; Sigma-Aldrich, D9891), respectively. To block PPP-family protein phosphatases, cells were treated with 50 nM Ok. Ac. (Sigma-Aldrich, O9381). To induce mitophagy, cells were treated with 10 μM Antimycin A (Sigma-Aldrich, A8674) and 5 μM Oligomycin A (Sigma-Aldrich, 75351) at the indicated time points. For lysosomal inhibition, cells were treated with 100 nM Bafilomycin A1 (Selleckchem, S1413) for 60 min or 50 nM for 4 hours. For TFEB nuclear translocation, cells were treated with 100 nM

Torin1 (Selleckchem, S2827) for 1 hour. Protein synthesis was inhibited with 50 μM cycloheximide (CHX; Sigma-Aldrich, C4859). Where indicated, cells were treated with 20 μM Q-VD-Oph (SelleckChem, S7311) to prevent cell death upon prolonged mitochondrial damage (*8*).

Lentivirus production and transduction

For lentivirus production, HEK293T cells were seeded in a culture dish (2.5 × 10^6 cells/100 mm) and transfected with 7 μg of plasmid DNA [mt-mKeima (*34*): gift from T. Finkel, National Heart Lung and Blood Institute, Bethesda, USA; RFP-GFP-FIS1 or cherry-Parkin (*36*): gift from F. Steinberg, Albert Ludwigs Universitaet Freiburg, Freiburg, Germany], 6 μg of PAX8 (packaging plasmid) and 5 μg of VSVG (envelope plasmid) for 7 hours using Lipofectamine 2000 (Thermo Fisher Scientific, 11668019) according to the manufacturer's protocol. Lentivirus was harvested 24 hours posttransfection, filtered (0.45 μm), diluted 1:2 in P/S-free medium, and supplemented with polybrene (10 μg/ml; hexadimethrine bromide, Sigma-Aldrich, H9268).

Small interfering RNA (siRNA) and plasmid transient transfection

Inducible HA-Parkin HeLa cells were transfected with 20 nM each small interfering RNA (siRNA) using Lipofectamine RNAiMAX (Thermo Fisher Scientific, 13778150) as described by the manufacturer, 48 hours before harvesting or treating the cells with the indicated reagents. SH-SY5Y cells were subjected to the same protocol of transfection but for two consecutive days.

siRNA sequences are as follows, with deoxythymidine dinucleotide 3′ overhangs (dT–dT tails):

1) siCTR (targeting mCherry/RFP; used in all experiments but in cells expressing mKeima/mCherry/RFP), sense: 5′-GCUCCAAGGCCUACGUGAAUU-3′.

2) siCTR (used in cells expressing mKeima/mCherry/RFP), sense: 5′-CGUACGCGGAAUACUUCGA-3′.

3) siB55α #1, sense: 5′-GCCUAGACUUCAAUAAGAA-3′.

4) siB55α #3, sense: 5′-UUCUUAUUGAAGUCUAGGC-3′.

5) siPINK1, sense: 5′-GCCAUCUUGAACACAAUGA-3′.

6) siPR65A/PPP2R1A, sense: 5′-CUUCGACAGUACUUCCGGA-3′.

7) siPR65B/PPP2R1B, sense: 5′-CUUCGACAGUACUUCCGGA-3′.

All siRNAs were validated in this study by immunoblot of the knocked-down protein. Transient transfections of Flag-TFEB-S142/211A (*42*) or HA-ULK1 (*59*) (gift from S. Tooze) were performed using GeneJuice transfection reagent (Sigma-Aldrich, 70967) according to the manufacturer's protocols.

λ-PP assay

Phosphatase assay was performed on protein extracts from Parkin-induced HeLa cells, lysed in radioimmunoprecipitation assay (RIPA) buffer, as described below, and diluted 1:3 in 1X NEBuffer for PMP, with or without λ-PP (New England Biolabs, P0753S). The reactions were incubated for 30 min at 30°C, and protein extracts were denatured and analyzed by immunoblot, as described in the relative section.

In vitro phosphatase assay with purified PP2Ac

Anti-HA immunoprecipitation was performed from HEK293 cells overexpressing HA-ULK1, as previously described (*60*). After incubation with anti-HA magnetic beads (Pierce, 88836), samples were washed twice in washing buffer and twice in PP assay buffer [50 mM Hepes (pH 7.5; Sigma-Aldrich, H7523), 100 mM NaCl (Sigma-Aldrich, S5886), 2 mM $MgCl_2$ (Sigma-Aldrich, M8266), 1 mM dithiothreitol (DTT; Merck-Millipore, 43819), and 0.5% NP-40 (Sigma-Aldrich, I8896)]. Samples were then split into two fractions: one fraction was left untreated (as a control), and the other was treated with 1 μl of purified PP2Ac (0.44 mg/ml; Cayman Chemical, 10011237). After incubation at 30°C for 30 min, samples were denatured with 4× Laemmli sample buffer (Thermo Fisher Scientific, NP0008), and immunoblot was performed as described below.

Biochemical purification of the B55α subunit

Protein purification workflow:

1) Cell lysis and clarification: A 20-ml cell pellet of starved ULK1/2 DKO MEF cells was lysed by douncing in 90 ml of buffer A [20 mM Hepes (pH 7.5), 10 mM NaCl, and 1 mM DTT]. The lysate was centrifuged at 12,000*g* for 10 min at 4°C. Next, the supernatant was further clarified by centrifugation at 100,000*g* for 1 hour at 4°C.

2) SP column (cation exchange chromatography): The clarified lysate was loaded onto an SP column, and the resulting flowthrough was collected for subsequent purification.

3) Heparin column (affinity chromatography): The SP column flowthrough was loaded onto a heparin column, and resulting heparin column flowthrough was collected for the next step.

4) Q column (anion exchange chromatography): The heparin column flowthrough was loaded onto a Q column, using buffers A [20 mM Hepes (pH 7.5), 10 mM NaCl, and 1 mM DTT] and B [20 mM Hepes (pH 7.5), 1000 mM NaCl, and 1 mM DTT]. The column was then washed with 15% buffer B and eluted with 35% buffer B.

5) Ammonium sulfate precipitation: Ammonium sulfate (Sigma-Aldrich, A4418) was added to the eluted sample to a final concentration of 20% and incubated at 4°C for 30 min, and precipitated proteins were removed by centrifugation at 47,800*g* for 10 min. The supernatant was diluted to 10% ammonium sulfate.

6) Phenyl sepharose column (hydrophobic interaction chromatography): The diluted sample was loaded onto a phenyl sepharose column, using buffers A [5 mM Hepes (pH 7.5) and 1 mM DTT] and B [20% ammonium sulfate, 20 mM Hepes (pH 7.5), 400 mM NaCl, and 1 mM DTT]. The column was eluted with a gradient of 50% to 0% buffer B across 20 fractions, which were dialyzed and assayed for activity.

7) Hydroxyapatite column (calcium phosphate chromatography): Active fractions were pooled and loaded onto a hydroxyapatite column, using buffers A [20 mM Hepes (pH 7.5), 10 mM NaCl, and 1 mM DTT] and B [1 M phosphate buffer (pH 7.5) and 1 mM DTT]. Next, the column was washed with 3% buffer B and eluted with a gradient of 3 to 18% buffer B across 20 fractions. The resulting fractions were dialyzed and assayed for activity.

8) Q column (anion exchange chromatography): Active fractions were concentrated using a Q column under the same buffer conditions as before.

9) Size exclusion chromatography (SEC): The concentrated sample was loaded onto a gel filtration column, and active fractions were combined.

10) Mono-Q column (high-resolution anion exchange chromatography): Active fractions were loaded onto a Mono-Q column, using the same buffer as the Q column. Next, the column was washed with 18% buffer B (180 mM NaCl) and eluted across a gradient of

19% buffer B (190 mM NaCl) to 34% buffer B (340 mM NaCl) in 20 × 1 ml fractions. Eight microliters of each fraction were assayed for activity.

SYPRO staining

SDS-PAGE of chromatography fractions was stained with SYPRO Ruby protein gel stain (Bio-Rad, 1703125), according to the manufacturer's instructions.

LC-MS of chromatography fractions

Sample preparation

Each fraction from SEC was separately reduced with 10 mM DTT (Sigma-Aldrich, 43815) and alkylated using 55 mM Iodoacetamide (Sigma-Aldrich, I1149); both reactions were carried out for 1 hour at room temperature (RT). Alkylated proteins were then submitted to a digestion using trypsin (Promega, V5113) overnight at 35°C. Digested peptides were desalted using StageTip (*61*) before injection into the mass spectrometer.

LC-MS analysis

Desalted peptides were separated by nanoscale C18 reverse-phase liquid chromatography performed on an EASY-nLC II (Thermo Fisher Scientific) coupled to an Orbitrap Elite mass spectrometer (Thermo Fisher Scientific). Elution was carried out using a binary gradient with buffer A: water (Merck-Millipore, 1.5333.1000) and B: 80% acetonitrile (VWR Chemical, 83640.320), both containing 0.1% of formic acid (Merck-Millipore, 1.00264.0100). Peptide mixtures were separated at flow rate of 300 nl/min, using a binary gradient into a 20-cm fused silica emitter (New Objective) packed in-house with ReproSil-Pur C18-AQ, 1.9-μm resin (Dr Maisch GmbH, r119 b9 0003), for a total run-time duration of 135 min. Packed emitter was kept at 35°C by means of a column oven integrated into the nanoelectrospray ion source (Sonation). An Active Background Ion Reduction Device was used to decrease ambient contaminant signal level.

General mass spectrometric conditions were as follows: spray voltage: 2.1 kV and ion transfer tube temperature: 200°C. The mass spectrometer was operated in positive ion mode and used in data-dependent acquisition (DDA) mode. A full scan (FT-MS) was acquired at a target value of 1,000,000 ions with resolution $R = 240,000$ over a mass range of 300 to 1700 amu. The top 15 most intense ions were selected for fragmentation in the dual linear ion trap using a maximum activation time of 10 ms or a target value of 30,000 ions. Multiply charged ions from two to four charges having intensity greater than 500 counts were selected through a 2-amu window and fragmented using normalized collision energy of 35. Former target ions selected for tandem MS were dynamically excluded for 60 s.

Data analysis

The MS raw files were processed with MaxQuant software (*62*) version 2.3.0.0 and searched with Andromeda search engine (*63*), querying UniProt (*64*) *Homo sapiens* (7 September 2016; 63,668 entries). The database was searched, requiring specificity for trypsin cleavage and allowing a maximum of two missed cleavages. Methionine oxidation and N-terminal acetylation were specified as variable modifications, and cysteine carbamidomethylation as fixed modification. The peptide, protein, and site false discovery rate (FDR) were set to 1%.

MaxQuant output "proteinGroups.txt" was further processed and analyzed using Perseus software version 1.6.15.063. The common reverse and contaminant hits (as defined in MaxQuant output) were removed. Only protein groups identified with at least one uniquely assigned peptide were used for the analysis.

For data visualization, a hierarchical clustering analysis on protein intensity columns was performed using "Euclidean distance" for both rows and columns. To maintain the order of the SEC elution, the columns were constrained using the "Preserve order" option.

Immunoblotting

Cells were washed twice with ice-cold phosphate-buffered saline (PBS) and lysed in RIPA buffer [50 mM tris-HCl (pH 7.5; Lonza, 51237), 1% Triton X-100 (Sigma-Aldrich, T8787), 0.25% sodium deoxycholate (Sigma-Aldrich, D6750), 150 mM NaCl, 0.2% SDS (Sigma-Aldrich, 436143), 5 mM $MgCl_2$, and 1 mM EDTA (Merck-Millipore, E9884)] containing protease (Sigma-Aldrich, P8340-5ML) and phosphatase inhibitors (Thermo Fisher Scientific, 78426) on ice for 20 min. Lysates were centrifuged at 16,000*g* at 4°C for 10 min, and supernatants were collected. Protein concentrations were determined by BCA Protein Assay Kit (Thermo Fisher Scientific, A55865). Samples were denatured by adding Laemmli buffer (Thermo Fisher Scientific, NP0008; supplemented with DTT) and heating at 95°C for 5 min. Proteins were separated on SDS-PAGE and transferred to polyvinylidene difluoride (PVDF) membranes (Bio-Rad, 1704273). Membranes were blocked with either 5% skim milk powder or with 3% bovine serum albumin (BSA; Sigma-Aldrich, A9418) in TBS-T [tris-buffered saline (TBS; Sigma-Aldrich, P2287) supplemented with 0.1% Tween 20 (Thermo Fisher Scientific, 28358)] for 1 hour at RT. The blots were incubated with the indicated primary antibodies in blocking solution overnight at 4°C. The next day, membranes were washed three times with TBS-T and incubated with horseradish peroxidase (HRP)–conjugated secondary antibodies (1:10,000 in blocking solution) for 1 hour at RT. Membranes were washed three times with TBS-T, and signals were detected using SuperSignal West Femto Maximum Sensitivity Substrate (Thermo Fisher Scientific, 34096) or Immobilon Western Chemiluminescent HRP Substrate (Merck-Millipore, WPKLS0500). Densitometric analysis was performed using Image Lab software. A full list of the antibodies used is provided in table S2.

Mitochondria-enriched cellular fractionations

Cells were resuspended in Sucrose Buffer [140 mM sucrose (Sigma-Aldrich, S9378), 420 mM Mannitol (Sigma-Aldrich, 63560), 10 mM tris, and 2 mM EGTA (Sigma-Aldrich, 324626)] supplemented with Protease and Phosphatase Inhibitor Cocktail (Thermo Fisher Scientific, 78440) and membranes disrupted by mechanical dissociation with 100-hit glass homogenizer (2-ml Potter-Elvehjem). Cells were then centrifuged twice for 10 min at 1000*g* to remove cell nuclei and debris. Supernatant was centrifuged at 12,000*g* for 15 min to separate the cytosolic fraction (supernatant) and the mitochondria-containing pellet. For immunoblotting, mitochondrial cell fractions were lysed in RIPA buffer (see above) plus Protease and Phosphatase Inhibitor Cocktail.

Immunofluorescence

Cells were grown on coverslips coated with Fibronectin (10 μg/ml; Sigma-Aldrich, F2006), treated as described in the figure legends, and then fixed with 4% formaldehyde (AppliChem, 131328.1211) for 15 min at RT. For LC3 staining, 4% formaldehyde fixation was followed by 10 min in ice-cold methanol at −20°C. Cells were permeabilized with 0.1% Triton X-100 in PBS for 5 min and blocked for

1 hour in a blocking solution containing 5% normal goat serum (Gibco, PCN5000) and 0.01% Triton X-100.

Cells were incubated with primary antibodies for 2 hours at RT, washed three times with PBS containing 0.01% Triton, and then incubated with Alexa Fluor 488 (Invitrogen, A11070)– or Alexa Fluor 568 (Invitrogen, A-11011)–conjugated secondary antibodies (diluted in PBS with 0.01% Triton) for 45 min at RT. Nuclei were stained with Hoechst 33342 (Thermo Fisher Scientific, H3570; 1:1000 in PBS), and cells were mounted using ProLong Gold Antifade mounting solution (Thermo Fisher Scientific, P36934). Images were acquired using a Zeiss LSM 800 confocal microscope (Zeiss, Oberkochen, Germany). A Z-series of optical sections was generated at 0.5-μm increments, and maximum intensity projections were created. Detectors were adjusted to capture optimal signal levels without reaching saturation. Image processing was performed using ImageJ software.

To quantify LC3-positive puncta, individual cells were manually outlined, and the same threshold was applied across all images. LC3 puncta were then quantified using the Analyze Particles plugin in ImageJ.

Colocalization analysis was performed to assess the overlap between Parkin and LC3, and Parkin and TOM20, in single z-stacks of individual cells. Images were analyzed in ImageJ using the JACoP (Just Another Colocalization Plugin) plugin. Pearson's correlation coefficient was calculated to quantify the degree of colocalization. Values close to +1 indicate high colocalization, values near 0 indicate random localization, and values close to −1 indicate mutually exclusive localization.

Mitochondria immunoisolation

Cells were rinsed once in cold PBS and collected in PBS by scraping. Cells were centrifuged for 5 min at 1500*g* at 4°C. Pellets were washed twice in 10-ml Mitochondrial Isolation Buffer (MIB)/Sucrose Mannitol Buffer (SuMa) [0.1 M Hepes, 1 M Mannitol, and 1 M Sucrose (pH adjusted to 7.5 with NaOH) (Sigma-Aldrich, S8045)] and centrifuged again for 5 min at 1500*g* at 4°C before lysis in MIB4/SuMa4 buffer [MIB/SuMa stock supplemented with 0.5 mM DTT, 0.5% fatty acid–free BSA (Sigma-Aldrich, 126575), mini complete protease inhibitor without EDTA, and 1 μl Benzonase (Sigma-Aldrich, E1014)]. A fraction of the sample was collected (input), and the lysate was incubated for 5 min on ice. The lysate was passed through a 25-gauge needle three times and centrifuged for 10 min at 1500*g*, and the supernatant was transferred to a fresh tube. Any remaining pellet was resuspended in MIB4 and passed through a needle eight times and centrifuged for 10 min at 1500*g*. The two supernatant fractions were combined and centrifuged for 15 min at 1500*g*. Another fraction of the samples was collected (light membrane fraction). Samples were then labeled with TOM20 antibody (Abcam, ab78547) or rabbit immunoglobulin G (IgG) isotype control (Thermo Fisher Scientific, 31235) for 45 min at 4°C on ice. Secondary anti-rabbit IgG microbeads (Miltenyi Biotech, 130-048-602) were washed in MIB4, added to the samples, and incubated for 1 hour at 4°C on ice. The MS columns (Miltenyi Biotec, 130-042-201) were equilibrated with MIB4. The TOM20-labeled organelle suspension was applied to the MS column, and the suspension was run through. The columns were then washed once in SuMa4 and twice in MIB$^+$/SuMa$^+$ (MIB/SuMa supplemented with 0.5 mM DTT and 0.5% fatty acid–free BSA). The columns were then removed from the separator and placed in 1.5-ml Eppendorf tubes on ice. SuMa$^+$ buffer was applied to the column to immediately flush out the fraction with the magnetically labeled organelles using the plunger. The eluate was collected and centrifuged at 21,000*g* at 4°C for 20 min. Last, the samples (whole cell, light membrane fraction, and organelle-immunoprecipitation product) were prepared for immunoblotting and separated by SDS-PAGE.

Mitophagy flow cytometry assay

For assessing mitophagy flux, mt-mKeima–expressing cells were treated with OA as indicated, collected by trypsinization, pelleted and resuspended in ice-cold 1× PBS without sodium and magnesium, and supplemented with 5 to 10% FBS. The samples were analyzed on LSRFortessa X-20 (Becton Dickinson Life Sciences) by first plotting side scatter (SSC-A) and forward scatter (FSC-A) to define the live-cell population and then excluding cell doublets by plotting FSC-H and FSC-A. In addition, mKeima-positive cells were gated on the basis of the negative control (untransduced parental cells). The mt-mKeima shift analysis was performed by exciting the cytoplasmic and lysosomal mKeima with violet (405 nm) and yellow/green (561 nm) lasers, respectively. Emission was collected for both laser excitations at 610 ± 10 nm simultaneously, for 25,000 events per sample, and for $n = 3$ biological replicates unless otherwise stated. All flow cytometry analyses were performed in FACSDiva software, available on LSRFortessa X-20.

Annexin V propidium iodide assay

Apoptosis analyses were performed with the APC annexin V kit (BD Biosciences, 550475) according to the manufacturer's protocol. Briefly, spent culture medium containing detached cells was collected, mixed with trypsinized cells, and centrifuged at 300*g* for 5 min. After washing once in ice-cold PBS, cells were incubated in annexin V Incubation reagent (1% APC annexin V; in 1× binding buffer) for 15 min in the dark. Five minutes before acquisition, propidium iodide (0.05 mg/ml; Thermo Fisher Scientific, P4864) was added to the samples.

Analysis of mitochondrial transmembrane potential

Total mitochondrial mass and mitochondrial transmembrane potential ($\Delta\psi$m) were analyzed by incubating cells with 50 nM MitoTracker Green FM (Thermo Fisher Scientific, M7514) or 200 nM MitoProbe TMRM Assay Kit (Thermo Fisher Scientific, M20036), respectively, in DMEM without serum and Phenol Red (Thermo Fisher Scientific, 21063029) for 30 min. Stained cells were washed twice with cold PBS, collected, and analyzed by flow cytometry (FACSVerse, BD Biosciences). Normalized $\Delta\psi$m was calculated as TMRM/MitoTracker Green FM relative fluorescence (geometric mean).

Immunofluorescence high-throughput microscopy, and quantitative image-based cytometry (QIBC)

HeLa cells were plated at the desired confluency and treated according to the experimental setup. After treatment, cells were fixed in 4% formaldehyde diluted in PBS (AppliChem, 131328.1211) and permeabilized with 0.5% Triton-X 100 for 5 min. Immunofluorescence staining was performed using TFEB antibody (Cell Signaling Technology, 37785) diluted 1:100 in a 2% BSA solution in PBS for 2 hours at RT. Alexa Fluor 488 (Invitrogen, A11070) was used as a secondary antibody, and last, cells were counterstained for nuclear segmentation with Hoechst.

Cells were imaged with Celldiscoverer 7 (Zeiss, Oberkochen, Germany) using a 20× magnification objective. After background subtraction and tile stitching, cells were segmented for cytoplasmic and nuclear area with arivis software using a customized pipeline implemented with cellpose algorithm (*65*).

Dataset from image analysis was processed with R (v 4.3.2). Each replicate was individually sliced in a randomized fashion (slice_sample function) to get 500 cells from each one. Plot was generated using the ggplot2 package, overlapping geom_jitter and geom_boxplot for data visualization. Five hundred randomly generated data points are shown (slice_sample function). Statistical analysis was performed with R (v 4.3.2), using aov function for one-way analysis of variance (ANOVA), followed by Tukey's post hoc test for multiple comparison.

Nucleus/cytosol fractionation

Cells were cultured in 100-mm dishes and treated with dimethyl sulfoxide (DMSO), OA for 4 hours, or Torin1 for 1 hour. Cells were washed in PBS, gently scraped, and centrifuged at 600*g* for 5 min at 4°C. Pellets were dried and lysed on ice with 100 μl of buffer A [10 mM Hepes (pH 8), 10 mM KCl (Sigma-Aldrich, P9541), 0.2 mM EDTA, 1 mM DTT, and 0.6% NP-40, supplemented with proteinase and phosphatase cocktail inhibitors]. Every 10 min, samples were vortexed. Then, cell lysates were centrifuged at 11,000*g* for 10 min at 4°C. Supernatants were collected while the remaining pellets were washed twice with 500 μl of buffer B (buffer A without NP-40, supplemented with proteinase and phosphatase cocktail inhibitors). After the second wash, pellets were dried, lysed in whole cell lysis buffer [50 mM tris-HCl (pH 6.8; UCS Diagnostic, THCL299), 10% Glycerol (Sigma-Aldrich, G6279) and 2% SDS (Sigma-Aldrich, 436143)], and boiled at 99°C for 10 min while shaking at maximum speed. Aliquots of the cytosolic and nuclear fractions were used to quantify protein concentration and denatured with Laemmli buffer.

RNA isolation and reverse transcription qPCR (RT-qPCR)

Total RNA was isolated from cultured cells using the NucleoSpin RNA Columns (Macherey-Nagel, DE, catalog no. 740955) according to the manufacturer's protocol. RNA concentration was quantitated by spectrophotometry, and 500 ng of total RNA was used for reverse transcription with M-MLV reverse transcriptase (Promega, WI, USA, catalog no. M1705) following the manufacturer's instructions. The resulting cDNA was diluted to 5 ng/μl and stored at −20°C. Reverse transcription qPCR (RT-qPCR) was performed using the ViiA 7 Real-Time PCR System v1.3 (Applied Biosystems, CA, USA) under optimized PCR conditions. Reactions (20 μl) containing 10 ng of cDNA were carried out in a 96-well plate using PowerUp SYBR Green Master Mix (Thermo Fisher Scientific, MA, USA, catalog no. A25742) according to the manufacturer's protocol, with forward and reverse primers for each gene. Each assay included a negative control and was run in triplicate. Data were normalized to β-2 microglobulin, and fold change was calculated using the $\Delta\Delta C_t$ method. Primer pairs, designed using Primer-BLAST, were as follows: PGC-1α, 5′-GCTACGAGGAATATCAGCACGA-3′ (forward); PGC-1α, 5′-ACACGGCGCTCTTCAATTG-3′ (reverse); TFAM, 5′-GGCAAGTTGTCCAAAGAAACC-3′ (forward); TFAM, 5′-GCATCTGGGTTCTGAGCTTTA-3′ (reverse); β-2 microglobulin, 5′-CTCCGTGGCCTTAGCTGTG-3′ (forward) and 5′-TCTCTGCTGGATGACGTGAG-3′ (reverse).

RNA sequencing

Parkin-induced HeLa cells were depleted for B55α (siB55α #1) or transfected with a nontargeting control oligo (siCTR), as described above, for 72 hours. RNA was isolated from three independent experiments using the NucleoSpin RNA Columns (Macherey-Nagel, DE, catalog no. 740955), and the samples were sequenced by the BGI DNBSEQ platform. Low-quality, adapter-polluted, and high content of unknown base (N) reads were removed from the pool, and clean reads were mapped to GRCh38/hg38 reference genome using HISAT264.

Functional analysis on transcriptomics data

The threshold for statistical significance of the differential expression analyses was FDR < 0.05. The differentially expressed genes (DEGs) were 4417, divided into 2141 induced and 2276 inhibited (table S3; DEGs). GOEA was performed on these genes, separately, using the DAVID Bioinformatic tool (*66*, *67*), restricting the output to CC (table S4; GOEA). The CLEAR site was searched using the TEFBexplorer web tool (https://tfeb.tigem.it) (*68*). The promoter region analyzed was 1000–base pair upstream and 200 downstream from the transcription start site for the human sequences (table S5; CLEAR). The Venn diagram shows that 1207 of 2276 genes are CLEAR-containing genes (Fig. 4E). The GOEA was also performed on the 1207 CLEAR-containing genes, restricting the output to CC terms and Kyoto Encyclopedia of Genes and Genomes (KEGG) pathways (*69*, *70*) (GOEA_CLEAR; table S6 and Fig. 4E). The threshold for statistical significance of GOEA was FDR < 0.1, and enrichment score ≥ 1.5, while for the KEGG pathway analyses, it was FDR < 0.1.

DNA isolation and qPCR-based mtDNA quantification

DNA was extracted using the E.Z.N.A. Tissue DNA Kit (Omega Bio-tek, catalog no. D3396), according to the manufacturer's instructions. qPCR was performed using the ViiA 7 Real-Time PCR System v1.3 (Applied Biosystems, CA, USA) under optimized PCR conditions. Reactions (20 μl) containing 25 and 5 ng of DNA for genomic β-ACTIN (gen-β-ACT) and the mitochondrial gene mtND1, respectively, were carried out in a 96-well plate using PowerUp SYBR Green Master Mix (Thermo Fisher Scientific, MA, USA, catalog no. A25742), according to the manufacturer's protocol, with forward and reverse primers for each gene. Each assay included a negative control and was run in triplicate. Data were normalized to genomic ACTIN, and fold change was calculated using the $\Delta\Delta C_t$ method. Primer pairs were as follows: gen-β-ACT, 5′- CCCCTGGCGGCCTAAGGACT-3′ (forward) and 5′- ACATGCCGGAGCCGTTGTCG-3′ (reverse); and mtND1, 5′- TTCTCCGATCCGTCCCTAACA-3′ (forward) and 5′-GGTTGTCCTCCGATTCAGGTT-3′ (reverse).

Real-time investigation of oxygen consumption rate

Mitochondrial respiratory states were analyzed in intact cells using the XF96e Extracellular Flux Analyzer and XFe96/XF Pro Cell Culture Microplates (Agilent, 103794-100). Cells were seeded into the XFe96/XF Pro Cell Culture Microplates at a density of 1×10^4 cells per well in growth medium 1 day before the experiment. Oxygen consumption rate (OCR) measurements were conducted at 37°C in Seahorse XF Media (Agilent, 103335-100) [containing 10 mM glucose (Sigma-Aldrich, 49163), 10 mM pyruvate (Sigma-Aldrich, S8636), and 2 mM glutamine (Agilent, 103579-100), at pH 7.4]. Key parameters, including mitochondrial respiratory states, respiratory control ratio, and coupling efficiency of oxidative phosphorylation, were assessed following a previously validated protocol (*71*, *72*). The following compounds and concentrations were used: oligomycin A (1 μM) (Sigma-Aldrich, 75351), carbonyl cyanide *p*-trifluoromethoxyphenylhydrazone (0.6 μM) (Sigma-Aldrich, C2920), antimycin A (2.5 μM) (Sigma-Aldrich, A8674), and rotenone (2.5 μM) (Sigma-Aldrich, R8875). After OCR measurements, data were normalized to cell numbers using the Celigo Cell Imaging Cytometer (Nexcelom Bioscience), as described previously (*72*).

Data analysis

Densitometric analysis using Fiji

Chemiluminescence signal from immunoblots was quantified using Fiji (v2.9.0). Individual bands were selected using the rectangle tool and using the Select First Lane and Select Next Lane tool (Analyze Gel Select First Lane/Select Next Lane). Then, the Plot Lanes function was applied (Analyze Gel Plot Lanes), and the straight line freehand tool used to segment off the peak intensity. Once segmented, the wand tool was used to detect band intensity. The raw intensity was normalized to the control sample and then normalized to the loading control protein.

Flow cytometry analysis

For analysis, the live-cell population was defined by plotting side scatter (SSC-A) and forward scatter (FSC-A). Doublet discrimination was done on the live-cell population, and plotting FSC-H and FSC-A and mKeima-positive cells were gated on the basis of the negative control. The live-cell gating, doublet discrimination, and gating for mKeima-positive cells were copied to the group. The mt-mKeima shift analysis was performed on the control sample by plotting violet (405 nm) and yellow/green (561 nm). Using the free-hand line selection tool, the lysosomal mKeima population was gated parallel to the densest part of the cloud. All flow cytometry analyses were performed in FACSDiva software, available on LSR-Fortessa X-20.

Statistical analysis and data reproducibility

Statistical analyses were performed with GraphPad Prism 9 software. All statistical parameters including the exact value of n, type of replicates, the statistical test, error bars, and significance are reported in the related figure legends. All experimental findings were verified in ≥3 independent experiments.

No statistical methods were used to predetermine the sample size. The experiments were not randomized, and the investigators were not blinded to allocation during experiments and outcome assessment. All the data behind the statistical analysis will be provided as source data.

Supplementary Materials

The PDF file includes:

Figs. S1 to S11
Legends for tables S1 to S6

Other Supplementary Material for this manuscript includes the following:

Tables S1 to S6

REFERENCES AND NOTES

1. I. Dikic, Z. Elazar, Mechanism and medical implications of mammalian autophagy. *Nat. Rev. Mol. Cell Biol.* **19**, 349–364 (2018).
2. J. N. S. Vargas, M. Hamasaki, T. Kawabata, R. J. Youle, T. Yoshimori, The mechanisms and roles of selective autophagy in mammals. *Nat. Rev. Mol. Cell Biol.* **24**, 167–185 (2023).
3. I. G. Ganley, A. Simonsen, Diversity of mitophagy pathways at a glance. *J. Cell Sci.* **135**, jcs259748 (2022).
4. A. Picca, J. Faitg, J. Auwerx, L. Ferrucci, D. D'Amico, Mitophagy in human health, ageing and disease. *Nat. Metab.* **5**, 2047–2061 (2023).
5. T. G. McWilliams, M. M. Muqit, PINK1 and Parkin: Emerging themes in mitochondrial homeostasis. *Curr. Opin. Cell Biol.* **45**, 83–91 (2017).
6. D. P. Narendra, R. J. Youle, The role of PINK1-Parkin in mitochondrial quality control. *Nat. Cell Biol.* **26**, 1639–1651 (2024).
7. A. Khaminets, C. Behl, I. Dikic, Ubiquitin-dependent and independent signals in selective autophagy. *Trends Cell Biol.* **26**, 6–16 (2016).
8. M. Lazarou, D. A. Sliter, L. A. Kane, S. A. Sarraf, C. Wang, J. L. Burman, D. P. Sideris, A. I. Fogel, R. J. Youle, The ubiquitin kinase PINK1 recruits autophagy receptors to induce mitophagy. *Nature* **524**, 309–314 (2015).
9. T. N. Nguyen, J. Sawa-Makarska, G. Khuu, W. K. Lam, E. Adriaenssens, D. Fracchiolla, S. Shoebridge, D. Bernklau, B. S. Padman, M. Skulsuppaisarn, R. S. J. Lindblom, S. Martens, M. Lazarou, Unconventional initiation of PINK1/Parkin mitophagy by optineurin. *Mol. Cell* **83**, 1693–1709.e9 (2023).
10. E. Itakura, C. Kishi-Itakura, I. Koyama-Honda, N. Mizushima, Structures containing Atg9A and the ULK1 complex independently target depolarized mitochondria at initial stages of Parkin-mediated mitophagy. *J. Cell Sci.* **125**, 1488–1499 (2012).
11. J. N. S. Vargas, C. Wang, E. Bunker, L. Hao, D. Maric, G. Schiavo, F. Randow, R. J. Youle, Spatiotemporal control of ULK1 activation by NDP52 and TBK1 during selective autophagy. *Mol. Cell* **74**, 347–362.e6 (2019).
12. T. N. Nguyen, B. S. Padman, J. Usher, V. Oorschot, G. Ramm, M. Lazarou, Atg8 family LC3/GABARAP proteins are crucial for autophagosome-lysosome fusion but not autophagosome formation during PINK1/Parkin mitophagy and starvation. *J. Cell Biol.* **215**, 857–874 (2016).
13. D. C. Chan, Mitochondrial dynamics and its involvement in disease. *Annu. Rev. Pathol.* **15**, 235–259 (2020).
14. N. Pfanner, B. Warscheid, N. Wiedemann, Mitochondrial proteins: From biogenesis to functional networks. *Nat. Rev. Mol. Cell Biol.* **20**, 267–284 (2019).
15. P. R. Jannig, P. A. Dumesic, B. M. Spiegelman, J. L. Ruas, SnapShot: Regulation and biology of PGC-1α. *Cell* **185**, 1444–1444.e1 (2022).
16. D. F. Egan, D. B. Shackelford, M. M. Mihaylova, S. Gelino, R. A. Kohnz, W. Mair, D. S. Vasquez, A. Joshi, D. M. Gwinn, R. Taylor, J. M. Asara, J. Fitzpatrick, A. Dillin, B. Viollet, M. Kundu, M. Hansen, R. J. Shaw, Phosphorylation of ULK1 (hATG1) by AMP-activated protein kinase connects energy sensing to mitophagy. *Science* **331**, 456–461 (2011).
17. W. Tian, W. Li, Y. Chen, Z. Yan, X. Huang, H. Zhuang, W. Zhong, Y. Chen, W. Wu, C. Lin, H. Chen, X. Hou, L. Zhang, S. Sui, B. Zhao, Z. Hu, L. Li, D. Feng, Phosphorylation of ULK1 by AMPK regulates translocation of ULK1 to mitochondria and mitophagy. *FEBS Lett.* **589**, 1847–1854 (2015).
18. R. C. Laker, J. C. Drake, R. J. Wilson, V. A. Lira, B. M. Lewellen, K. A. Ryall, C. C. Fisher, M. Zhang, J. J. Saucerman, L. J. Goodyear, M. Kundu, Z. Yan, Ampk phosphorylation of Ulk1 is required for targeting of mitochondria to lysosomes in exercise-induced mitophagy. *Nat. Commun.* **8**, 548 (2017).
19. C. M. Hung, P. S. Lombardo, N. Malik, S. N. Brun, K. Hellberg, J. L. Van Nostrand, D. Garcia, J. Baumgart, K. Diffenderfer, J. M. Asara, R. J. Shaw, AMPK/ULK1-mediated phosphorylation of Parkin ACT domain mediates an early step in mitophagy. *Sci. Adv.* **7**, eabg4544 (2021).
20. M. Swingle, L. Ni, R. E. Honkanen, Small-molecule inhibitors of Ser/Thr protein phosphatases: Specificity, use and common forms of abuse. *Methods Mol. Biol.* **365**, 23–38 (2007).
21. P.-M. Wong, Y. Feng, J. Wang, R. Shi, X. Jiang, Regulation of autophagy by coordinated action of mTORC1 and protein phosphatase 2A. *Nat. Commun.* **6**, 8048 (2015).
22. Z. Hu, D. S. Sankar, B. Vu, A. Leytens, C. Vionnet, W. Wu, M. Stumpe, E. Martínez-Martínez, B. Stork, J. Dengjel, ULK1 phosphorylation of striatin activates protein phosphatase 2A and autophagy. *Cell Rep.* **36**, 109762 (2021).
23. D. M. Virshup, S. Shenolikar, From promiscuity to precision: Protein phosphatases get a makeover. *Mol. Cell* **33**, 537–545 (2009).
24. M. Mumby, The 3D structure of protein phosphatase 2A: New insights into a ubiquitous regulator of cell signaling. *ACS Chem. Biol.* **2**, 99–103 (2007).
25. V. Janssens, S. Longin, J. Goris, PP2A holoenzyme assembly: In cauda venenum (the sting is in the tail). *Trends Biochem. Sci.* **33**, 113–121 (2008).
26. B. A. Hemmings, C. Adams-Pearson, F. Maurer, P. Müller, J. Goris, W. Merlevede, J. Hofsteenge, S. R. Stone, Alpha- and beta-forms of the 65-kDa subunit of protein phosphatase 2A have a similar 39 amino acid repeating structure. *Biochemistry* **29**, 3166–3173 (1990).
27. B. Richter, D. A. Sliter, L. Herhaus, A. Stolz, C. Wang, P. Beli, G. Zaffagnini, P. Wild, S. Martens, S. A. Wagner, R. J. Youle, I. Dikic, Phosphorylation of OPTN by TBK1 enhances its binding to Ub chains and promotes selective autophagy of damaged mitochondria. *Proc. Natl. Acad. Sci. U.S.A.* **113**, 4039–4044 (2016).
28. J. Kim, M. Kundu, B. Viollet, K.-L. Guan, AMPK and mTOR regulate autophagy through direct phosphorylation of Ulk1. *Nat. Cell Biol.* **13**, 132–141 (2011).

29. F. Koyano, K. Okatsu, H. Kosako, Y. Tamura, E. Go, M. Kimura, Y. Kimura, H. Tsuchiya, H. Yoshihara, T. Hirokawa, T. Endo, E. A. Fon, J. F. Trempe, Y. Saeki, K. Tanaka, N. Matsuda, Ubiquitin is phosphorylated by PINK1 to activate parkin. *Nature* **510**, 162–166 (2014).
30. A. Kazlauskaite, C. Kondapalli, R. Gourlay, D. G. Campbell, M. S. Ritorto, K. Hofmann, D. R. Alessi, A. Knebel, M. Trost, M. M. K. Muqit, Parkin is activated by PINK1-dependent phosphorylation of ubiquitin at Ser^{65}. *Biochem. J.* **460**, 127–139 (2014).
31. F. M. Lopes, R. Schröder, M. L. C. J. da Frota, A. Zanotto-Filho, C. B. Müller, A. S. Pires, R. T. Meurer, G. D. Colpo, D. P. Gelain, F. Kapczinski, J. C. F. Moreira, M. da Cruz Fernandes, F. Klamt, Comparison between proliferative and neuron-like SH-SY5Y cells as an in vitro model for Parkinson disease studies. *Brain Res.* **1337**, 85–94 (2010).
32. J. M. Heo, N. J. Harper, J. A. Paulo, M. Li, Q. Xu, M. Coughlin, S. J. Elledge, J. Wade Harper, Integrated proteogenetic analysis reveals the landscape of a mitochondrial-autophagosome synapse during PARK2-dependent mitophagy. *Sci. Adv.* **5**, eaay4624 (2019).
33. J. M. Heo, A. Ordureau, J. A. Paulo, J. Rinehart, J. W. Harper, The PINK1-PARKIN mitochondrial ubiquitylation pathway drives a program of OPTN/NDP52 recruitment and TBK1 activation to promote mitophagy. *Mol. Cell* **60**, 7–20 (2015).
34. N. Sun, D. Malide, J. Liu, I. I. Rovira, C. A. Combs, T. Finkel, A fluorescence-based imaging method to measure in vitro and in vivo mitophagy using mt-Keima. *Nat. Protoc.* **12**, 1576–1587 (2017).
35. R. Rudolf, S. Trajanovska, D. G. Allen, T. Pozzan, In vivo monitoring of Ca^{2+} uptake into subcellular compartments of mouse skeletal muscle. *Methods Mol. Biol.* **1925**, 127–142 (2019).
36. A. Jimenez-Orgaz, A. Kvainickas, H. Nägele, J. Denner, S. Eimer, J. Dengjel, F. Steinberg, Control of RAB7 activity and localization through the retromer-TBC1D5 complex enables RAB7-dependent mitophagy. *EMBO J.* **37**, 235–254 (2018).
37. C. L. Nezich, C. Wang, A. I. Fogel, R. J. Youle, MiT/TFE transcription factors are activated during mitophagy downstream of Parkin and Atg5. *J. Cell Biol.* **210**, 435–450 (2015).
38. J. A. Martina, R. Puertollano, Protein phosphatase 2A stimulates activation of TFEB and TFE3 transcription factors in response to oxidative stress. *J. Biol. Chem.* **293**, 12525–12534 (2018).
39. M. Uhlen, C. Zhang, S. Lee, E. Sjöstedt, L. Fagerberg, G. Bidkhori, R. Benfeitas, M. Arif, Z. Liu, F. Edfors, K. Sanli, K. von Feilitzen, P. Oksvold, E. Lundberg, S. Hober, P. Nilsson, J. Mattsson, J. M. Schwenk, H. Brunnström, B. Glimelius, T. Sjöblom, P.-H. Edqvist, D. Djureinovic, P. Micke, C. Lindskog, A. Mardinoglu, F. Ponten, A pathology atlas of the human cancer transcriptome. *Science* **357**, eaan2507 (2017).
40. D. L. Medina, C. Settembre, A. Ballabio, Methods to monitor and manipulate TFEB activity during autophagy. *Methods Enzymol.* **588**, 61–78 (2017).
41. C. Settembre, C. Di Malta, V. A. Polito, M. Garcia Arencibia, F. Vetrini, S. Erdin, S. U. Erdin, T. Huynh, D. Medina, P. Colella, M. Sardiello, D. C. Rubinsztein, A. Ballabio, TFEB links autophagy to lysosomal biogenesis. *Science* **332**, 1429–1433 (2011).
42. C. Settembre, R. Zoncu, D. L. Medina, F. Vetrini, S. Erdin, S. Erdin, T. Huynh, M. Ferron, G. Karsenty, M. C. Vellard, V. Facchinetti, D. M. Sabatini, A. Ballabio, A lysosome-to-nucleus signalling mechanism senses and regulates the lysosome via mTOR and TFEB. *EMBO J.* **31**, 1095–1108 (2012).
43. J. A. Martina, Y. Chen, M. Gucek, R. Puertollano, MTORC1 functions as a transcriptional regulator of autophagy by preventing nuclear transport of TFEB. *Autophagy* **8**, 903–914 (2012).
44. A. Roczniak-Ferguson, C. S. Petit, F. Froehlich, S. Qian, J. Ky, B. Angarola, T. C. Walther, S. M. Ferguson, The transcription factor TFEB links mTORC1 signaling to transcriptional control of lysosome homeostasis. *Sci. Signal.* **5**, ra42 (2012).
45. J.-H. Shin, H. S. Ko, H. Kang, Y. Lee, Y.-I. Lee, O. Pletinkova, J. C. Troconso, V. L. Dawson, T. M. Dawson, PARIS (ZNF746) repression of PGC-1α contributes to neurodegeneration in Parkinson's disease. *Cell* **144**, 689–702 (2011).
46. J. C. Greene, A. J. Whitworth, I. Kuo, L. A. Andrews, M. B. Feany, L. J. Pallanck, Mitochondrial pathology and apoptotic muscle degeneration in *Drosophila parkin* mutants. *Proc. Natl. Acad. Sci. U.S.A.* **100**, 4078–4083 (2003).
47. J. Park, S. B. Lee, S. Lee, Y. Kim, S. Song, S. Kim, E. Bae, J. Kim, M. Shong, J.-M. Kim, J. Chung, Mitochondrial dysfunction in *Drosophila PINK1* mutants is complemented by *parkin*. *Nature* **441**, 1157–1161 (2006).
48. B. Lacroix, T. Lorca, A. Castro, Structural, enzymatic and spatiotemporal regulation of PP2A-B55 phosphatase in the control of mitosis. *Front. Cell Dev. Biol.* **10**, 967909 (2022).
49. J. S. Wasserman, B. Faezov, K. R. Patel, A. M. Kurimchak, S. M. Palacio, D. J. Glass, H. Fowle, B. C. McEwan, Q. Xu, Z. Zhao, L. Cressey, N. Johnson, J. S. Duncan, A. N. Kettenbach, R. L. J. Dunbrack, X. Graña, FAM122A ensures cell cycle interphase progression and checkpoint control by inhibiting B55α/PP2A through helical motifs. *Nat. Commun.* **15**, 5776 (2024).
50. L. Fan, M.-H. Liu, M. Guo, C.-X. Hu, Z.-W. Yan, J. Chen, G.-Q. Chen, Y. Huang, FAM122A, a new endogenous inhibitor of protein phosphatase 2A. *Oncotarget* **7**, 63887–63900 (2016).
51. D. L. Medina, S. Di Paola, I. Peluso, A. Armani, D. De Stefani, R. Venditti, S. Montefusco, A. Scotto-Rosato, C. Prezioso, A. Forrester, C. Settembre, W. Wang, Q. Gao, H. Xu, M. Sandri, R. Rizzuto, M. A. De Matteis, A. Ballabio, Lysosomal calcium signalling regulates autophagy through calcineurin and TFEB. *Nat. Cell Biol.* **17**, 288–299 (2015).
52. N. Moradi, V. C. Sanfrancesco, S. Champsi, D. A. Hood, Regulation of lysosomes in skeletal muscle during exercise, disuse and aging. *Free Radic. Biol. Med.* **225**, 323–332 (2024).
53. L. Esteban-Martínez, E. Sierra-Filardi, R. S. McGreal, M. Salazar-Roa, G. Mariño, E. Seco, S. Durand, D. Enot, O. Graña, M. Malumbres, A. Cvekl, A. M. Cuervo, G. Kroemer, P. Boya, Programmed mitophagy is essential for the glycolytic switch during cell differentiation. *EMBO J.* **36**, 1688–1706 (2017).
54. Y. Lee, D. A. Stevens, S.-U. Kang, H. Jiang, Y.-I. Lee, H. S. Ko, L. A. Scarffe, G. E. Umanah, H. Kang, S. Ham, T.-I. Kam, K. Allen, S. Brahmachari, J. W. Kim, S. Neifert, S. P. Yun, F. C. Fiesel, W. Springer, V. L. Dawson, J.-H. Shin, T. M. Dawson, PINK1 primes Parkin-mediated ubiquitination of PARIS in dopaminergic neuronal survival. *Cell Rep.* **18**, 918–932 (2017).
55. S. K. Pirooznia, C. Yuan, M. R. Khan, S. S. Karuppagounder, L. Wang, Y. Xiong, S. U. Kang, Y. Lee, V. L. Dawson, T. M. Dawson, PARIS induced defects in mitochondrial biogenesis drive dopamine neuron loss under conditions of parkin or PINK1 deficiency. *Mol. Neurodegener.* **15**, 17 (2020).
56. J. P. Hardee, M. K. Caldow, A. S. M. Chan, S. K. Plenderleith, J. Trieu, R. Koopman, G. S. Lynch, Dystrophin deficiency disrupts muscle clock expression and mitochondrial quality control in mdx mice. *Am. J. Physiol. Cell Physiol.* **321**, C288–C296 (2021).
57. J. M. Memme, M. Slavin, N. Moradi, D. A. Hood, Mitochondrial bioenergetics and turnover during chronic muscle disuse. *Int. J. Mol. Sci.* **22**, 5179 (2021).
58. E. P. T. Hertz, T. Kruse, N. E. Davey, B. López-Méndez, J. O. Sigurðsson, G. Montoya, J. V. Olsen, J. Nilsson, A conserved motif provides binding specificity to the PP2A-B56 phosphatase. *Mol. Cell* **63**, 686–695 (2016).
59. E. Y. W. Chan, A. Longatti, N. C. McKnight, S. A. Tooze, Kinase-inactivated ULK proteins inhibit autophagy via their conserved C-terminal domains using an Atg13-independent mechanism. *Mol. Cell. Biol.* **29**, 157–171 (2009).
60. V. Cianfanelli, C. Fuoco, M. Lorente, M. Salazar, F. Quondamatteo, P. F. Gherardini, D. De Zio, F. Nazio, M. Antonioli, M. D'Orazio, T. Skobo, M. Bordi, M. Rohde, L. Dalla Valle, M. Helmer-Citterich, C. Gretzmeier, J. Dengjel, G. M. Fimia, M. Piacentini, S. Di Bartolomeo, G. Velasco, F. Cecconi, AMBRA1 links autophagy to cell proliferation and tumorigenesis by promoting c-Myc dephosphorylation and degradation. *Nat. Cell Biol.* **17**, 20–30 (2015).
61. J. Rappsilber, M. Mann, Y. Ishihama, Protocol for micro-purification, enrichment, pre-fractionation and storage of peptides for proteomics using StageTips. *Nat. Protoc.* **2**, 1896–1906 (2007).
62. J. Cox, M. Mann, MaxQuant enables high peptide identification rates, individualized p.p.b.-range mass accuracies and proteome-wide protein quantification. *Nat. Biotechnol.* **26**, 1367–1372 (2008).
63. J. Cox, N. Neuhauser, A. Michalski, R. A. Scheltema, J. V. Olsen, M. Mann, Andromeda: A Peptide Search Engine Integrated into the MaxQuant Environment. *J. Proteome Res.* **10**, 1794–1805 (2011).
64. The UniProt Consortium, UniProt: The universal protein knowledgebase. *Nucleic Acids Res.* **46**, 2699 (2018).
65. C. Stringer, T. Wang, M. Michaelos, M. Pachitariu, Cellpose: A generalist algorithm for cellular segmentation. *Nat. Methods* **18**, 100–106 (2020).
66. D. W. Huang, B. T. Sherman, R. A. Lempicki, Bioinformatics enrichment tools: Paths toward the comprehensive functional analysis of large gene lists. *Nucleic Acids Res.* **37**, 1–13 (2009).
67. D. W. Huang, B. T. Sherman, R. A. Lempicki, Systematic and integrative analysis of large gene lists using DAVID bioinformatics resources. *Nat. Protoc.* **4**, 44–57 (2009).
68. R. De Cegli, D. Carrella, D. Siciliano, G. Gambardella, G. Napolitano, C. Di Malta, A. Ballabio, D. di Bernardo, TFEBexplorer: An integrated tool to study genes regulated by the stress-responsive transcription factor EB. *Autophagy Rep.* **1**, 295–305 (2022).
69. M. Kanehisa, S. Goto, Y. Sato, M. Furumichi, M. Tanabe, KEGG for integration and interpretation of large-scale molecular data sets. *Nucleic Acids Res.* **40**, D109–D114 (2012).
70. M. Kanehisa, S. Goto, KEGG: Kyoto Encyclopedia of Genes and Genomes. *Nucleic Acids Res.* **28**, 27–30 (2000).
71. M. D. Brand, D. G. Nicholls, Assessing mitochondrial dysfunction in cells. *Biochem. J.* **435**, 297–312 (2011).
72. A. Hall, S. Maynard, L.-P. Wu, J. M. Merchut-Maya, R. Strauss, S. M. Moghimi, J. Bartek, Perturbation of mitochondrial bioenergetics by polycations counteracts resistance to BRAF(E600) inhibition in melanoma cells. *J. Control. Release Off. J. Control. Release* **309**, 158–172 (2019).
73. R. Edgar, M. Domrachev, A. E. Lash, Gene expression omnibus: NCBI gene expression and hybridization array data repository. *Nucleic Acids Res.* **30**, 207–210 (2002).
74. E. W. Deutsch, N. Bandeira, Y. Perez-Riverol, V. Sharma, J. J. Carver, L. Mendoza, D. J. Kundu, S. Wang, C. Bandla, S. Kamatchinathan, S. Hewapathirana, B. S. Pullman, J. Wertz, Z. Sun, S. Kawano, S. Okuda, Y. Watanabe, B. MacLean, M. J. MacCoss, Y. Zhu, Y. Ishihama, J. A. Vizcaíno, The ProteomeXchange Consortium at 10 years: 2023 update. *Nucleic Acids Res.* **51**, D1539–D1548 (2023).

75. Y. Perez-Riverol, J. Bai, C. Bandla, D. García-Seisdedos, S. Hewapathirana, S. Kamatchinathan, D. J. Kundu, A. Prakash, A. Frericks-Zipper, M. Eisenacher, M. Walzer, S. Wang, A. Brazma, J. A. Vizcaíno, The PRIDE database resources in 2022: A hub for mass spectrometry-based proteomics evidences. *Nucleic Acids Res.* **50**, D543–D552 (2022).

Acknowledgments: We thank V. Turcanova, at the Danish Cancer Institute, for the technical help and L. Di Leo for providing us with the protocol for the mtDNA quantification. **Funding:** F.C. laboratories and this work are supported by the European Union - Next Generation EU - NRRP M6C2 - Investment 2.1 Enhancement and strengthening of biomedical research in the NHS, project "Adenylosuccinate lyase deficiency, purine metabolism disorders and mitochondrial homeostasis: unveiling novel mechanisms to design therapeutic opportunities", ID project: PNRR-MR1-2022-12376821, the Italian Ministry of Health (RF-2019-12369700), AIRC (IG23543), Novo Nordisk (NNF24OC0094651), Danmarks Grundforskningsfond (DNRF125), the Italian Ministry of University and Research - MUR (PRIN 2017FS5SHL and 2020PKLEPN). V.C. is supported by the Italian Ministry of Health (GR-2021-12372771), the MUR (project ID: P2022TJZYZ; title: "Post-translational and transcriptional regulation of peroxisome turnover in health and disease," funded by the European Union - Next Generation EU, Piano Nazionale di Ripresa e Resilienza, Mission 4, Component 2, Investment 1.1, Progetti di Ricerca di Rilevante Interesse Nazionale PRIN 2022 – MUR, CUP F53D23008670001; MUR-Italy Departments of Excellence 2023-2027 to the Dept. of Science, Univ. Roma Tre), and was supported by "Fondazione U. Veronesi". G.M. and A.B. are supported by Horizon-MSCA-2022 Postdoctoral Fellowship (101108184) and Fondazione U. Veronesi, respectively. J.B. and A.H. are supported by grants from the Danish Cancer Society (R322-A17482), the Novo Nordisk Foundation (NNF20OC0060590), and the Swedish Research Council (VR-MH 2014-46602-117891-30). S.Z. is supported by Cancer Research UK (CRUK) Scotland Institute core funding to Advanced Technology Facilities (A17196) and CRUK Scotland Institute core funding awarded (A29800). **Author contributions:** Conceptualization: V.Ci., M.C., J.B., F.L., E.Z., and F.C. Methodology: V.Ci., S.M., R.D.C., S.L., A.H., M.B., K.M., S.I., S.Z., and E.Z. Investigation: V.Ci., M.N., S.C., S.M., D.S., S.L., R.D.C., M.B., C.F., M.P., V.Cl., G.M., A.H., E.G., M.S., A.B., G.C., C.D.M., and E.Z. Validation: V.Ci., M.N., A.H., M.C., T.P., S.Z., and E.Z. Formal analysis: V.Ci., D.S., S.L., M.B., R.D.C., A.H., G.M., E.G., M.S., and E.Z. Visualization: V.Ci., S.L., R.D.C., A.H., G.M., and F.C. Supervision: V.Ci., E.Z., J.B., K.M., A.M.-M., S.I., S.Z., E.Z., and F.C. Resources: V.Ci., S.L., S.I., K.M., F.L., J.B., C.D.M., S.Z., E.Z., and F.C. Project administration: V.Ci. and F.C. Funding acquisition: V.Ci., J.B., and F.C. Data curation: V.Ci., R.D.C., A.H., S.L., and J.B. Writing—original draft: V.Ci., R.D.C., F.L., and F.C. Writing—review and editing: V.Ci., M.N., D.S., R.D.C., M.B., G.M., A.H., M.P., V.Cl., E.G., M.S., A.B., G.C., M.C., T.P., K.M., A.M.-M., J.B., F.L., S.Z., S.I., E.Z., and F.C. **Competing interests:** The authors declare that they have no competing interests. **Data and materials availability:** Generated sequencing datasets are available at Gene Expression Omnibus (*73*) and are accessible through GEO Series accession number GSE307113 (www.ncbi.nlm.nih.gov/geo/query/acc.cgi?acc=GSE307113). The raw files and the MaxQuant search results files from the MS proteomics data have been deposited to the ProteomeXchange Consortium (*74*) via the PRIDE partner repository (*75*) with the dataset identifier PXD065566. All additional data needed to evaluate the conclusions in the paper are present in the paper and/or the Supplementary Materials.

Submitted 21 February 2025
Accepted 5 September 2025
Published 3 October 2025
10.1126/sciadv.adw7376